# Defect–Domain Wall Interactions in Trigonal Ferroelectrics

## Venkatraman Gopalan,[1] Volkmar Dierolf,[2] and David A. Scrymgeour[3]

[1] Department of Materials Science and Engineering, Pennsylvania State University, University Park, Pennsylvania 16802; email: vgopalan@psu.edu

[2] Department of Physics, Lehigh University, Bethlehem, Pennsylvania 18015

[3] Surface and Interface Sciences, Sandia National Laboratory, Albuquerque, New Mexico 98185-1415

## Key Words

ferroelectric domain walls, defect clusters, domain wall width, near-field scanning optical microscopy, piezoelectric force microscopy, Raman spectroscopy, rare-earth designer defects, X-ray synchrotron imaging

## Abstract

Domains and domain walls are a fundamental property of interest in ferroelectrics, magnetism, ferroelastics, superconductors, and multiferroic materials. Unlike magnetic Bloch walls, ideal ferroelectric domain walls are well accepted to be only one to two lattice units wide, over which polarization and strain change across the wall. However, walls in real ferroelectrics appear to show unexpected property variations in the vicinity of domain walls that can extend over micrometer length scales. This chapter specifically reviews the local electrical, elastic, optical, and structural properties of antiparallel domain walls in the trigonal ferroelectrics lithium niobate and lithium tantalate. It is shown that extrinsic point defects and their clustering play a key role in the observed local wall structure and influence macroscale properties by orders of magnitude. The review also raises broader and yet unexplored fundamental questions regarding intrinsic widths, defect–domain wall interactions, and static versus dynamic wall structure.

# 1. INTRODUCTION AND MOTIVATION FOR THE REVIEW

Ferroelectric materials have a built-in spontaneous polarization, $P_s$ (in units of electrical dipole moments per unit volume, C-m m$^{-3}$), in their crystal lattice in a certain range of temperatures and isotropic pressures when there is no external electric field (1). This spontaneous polarization has two or more orientational states and can be switched from one state to the other by an external electric field or, in some cases, by a mechanical stress. Regions in a ferroelectric with uniform polarization, $P$, are called ferroelectric domains. When two domains with $+P$ and $-P$ meet commensurately (i.e., with no mechanical discontinuity) within a crystal, they form domain walls that separate the two domains. All ferroelectrics can possess 180° domain walls (or antiparallel domain walls) that separate $+P$ and $-P$ polarization domains. For all the uniaxial ferroelectric crystals, to which we restrict this review, the polarization, $P_3$, can exist only along their crystallographic $c$ axis (also labeled as $3$, $x_3$, or $z$ axis in crystal physics coordinates). Thus, only 180° walls can exist in these materials. The technology surrounding ferroelectric domains is diverse (2–4), covering nonvolatile memory, piezoelectric actuators, ultrasound transducers, pyroelectric detectors, and surface acoustic wave devices as well as electro-optic and nonlinear optical applications. **Figure 1** shows a number of these applications that involve shaping ferroelectric domains and domain walls. Hence, an understanding of the local structure and dynamics of ferroelectric domain walls on the nano- and atomic scales and how it influences macroscale material properties is important for shaping ferroelectric domains.

In contrast to ferromagnetic domain walls, also called Bloch walls (5), in which the magnetic polarization can rotate continuously across a Bloch wall from one orientation to another, the strong coupling between ferroelectric polarization and lattice strain restricts the polarization in ferroelectrics to specific crystallographic directions. Ginzburg-Landau-Devonshire (GLD) phenomenological models describe abrupt polarization profiles in a continuum model as kinks or solitons (6–8). First-principles calculations predict that ideal ferroelectric walls are extremely narrow, typically on the order of one to two lattice units (9–11). Furthermore, because the lattice polarization is coupled to the spontaneous lattice strain through electrostriction, the local spontaneous strain width arising from the polarization gradient across such domain walls is expected to be sharp as well (12–14). The primary means of investigating wall widths on the unit cell level has been transmission electron microscopy (TEM) (12, 15–17). However, because the atomic displacements across an antiparallel wall are on the order of 0.02 nm, direct imaging and interpretation are still a challenge. Also, TEM may not be sensitive to subtle changes in material property across the wall on larger length scales. For twinned 90° walls, wall widths of ∼1.5 nm have been determined by measuring surface topography via atomic force microscopy (AFM) (14).

However, the recent literature points to a much richer local structure of an antiparallel wall in LiNbO$_3$, with unexpected optical birefringence (18, 19), strain (20, 21), local electric fields (22), and electromechanical contrast (23) that extend from ∼5 nm to 50 μm in the vicinity of the wall (24, 25). One may conclude from all the known literature that there is a range of length scales from unit cell level to micrometers over which the presence of a wall and its interaction with point defects influence the lattice
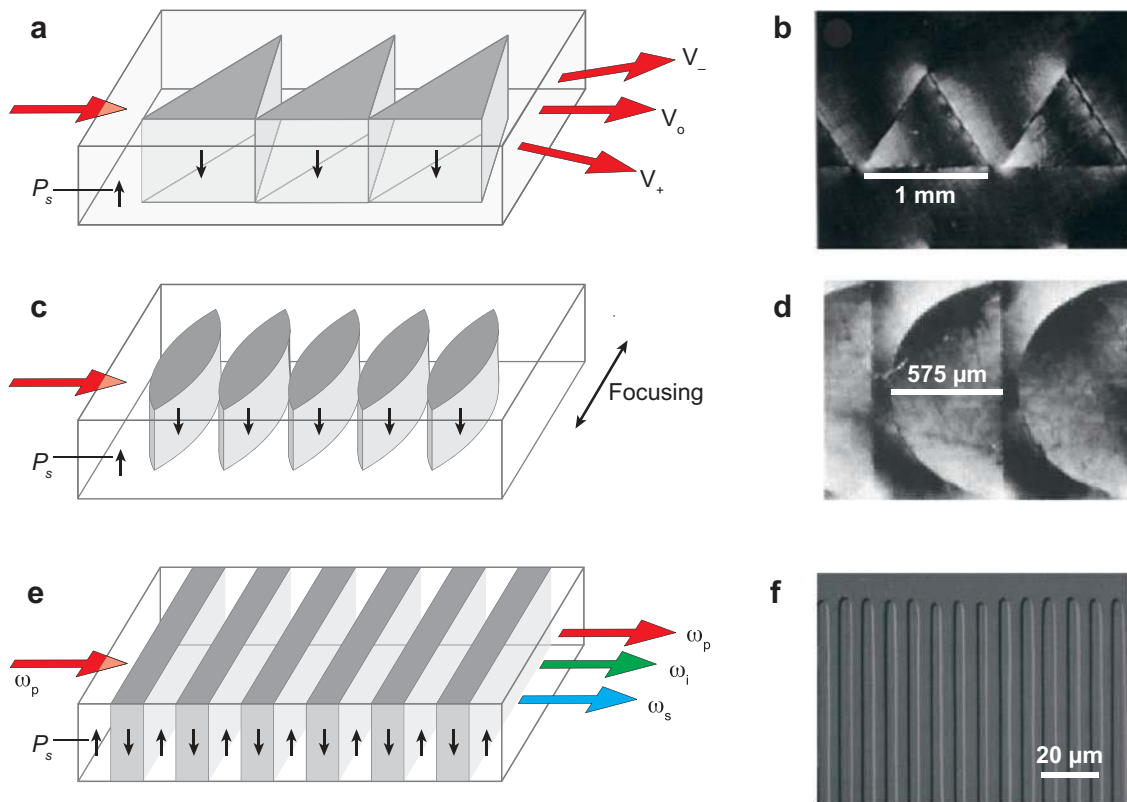
**Figure 1**

Examples of domain-engineered devices in single-crystal ferroelectric lithium niobate
($LiNbO_3$). (*a*) Schematic of an analog deflector that deflects light off an axis with applied bias.
(*b*) A series of domain-inverted triangles for laser deflection in lithium tantalate ($LiTaO_3$).
Reprinted from Reference 3, with permission from The Optical Society of America.
(*c*) Schematic of a dynamic focusing lens stack that can focus or defocus light in the plane.
(*d*) Planar view of a lens stack domain structure under crossed polarizers. Reprinted from
Reference 123, with permission from IEEE. Copyright 1997, IEEE. (*e*) Schematic of a
quasi-phase-matched (QPM) device in which the input beam $\omega_p$ is converted to a signal and
idler at $\omega_s$ and $\omega_i$. (*f*) Periodically poled structures with a QPM period of 8.0 μm in
1-mm-thick 1.0 mol% MgO-doped stoichiometric $LiTaO_3$. Reprinted from Reference 124,
with permission from Elsevier.

around it. It therefore becomes very important to define precisely what one means by
a domain wall width: whether in terms of a polarization gradient across the wall or of
a range of material properties that might be influenced by the presence of the wall.

Why is the problem of domain wall broadening important? Kim et al. (26) re-
cently showed that a broader domain wall dramatically lowers the coercive fields in
ferroelectrics. Bandyopadhyay & Ray (27), developing this idea further via perturba-
tion analysis, derived the range of stability of domain wall widths. Their low limit of
wall width (stable wall) agrees well with first-principles calculations, and the upper

limit (unstable wall) is in the range of 100 nm, similar to that measured by scanning probe microscopy (SPM) (23, 26). Theory that predicts narrow walls also predicts that defects can locate at and pin domain walls by creating additional dipolar and strain fields (9, 28, 29). Indeed, experiments show that domain walls can bend and bow under a field an order of magnitude smaller than the coercive field of the ferroelectric (18), indicating that coercive field may be a threshold for a pinning-depinning transition. Finally, the wall width may not be a static entity but rather one that may alter as the applied electric field approaches the coercive field. The key to answering these fundamental questions of very broad consequences to the field is to look closely at the static and dynamic wall widths.

## 2. CASE STUDY IN UNIAXIAL TRIGONAL FERROELECTRICS

This review specifically focuses on antiparallel walls in lithium niobate ($LiNbO_3$) and lithium tantalate ($LiTaO_3$), both of which are uniaxial trigonal ferroelectrics. These materials are widely used optical ferroelectrics today (2). The domain walls in these materials typify many broader issues in local domain wall structure and defect-wall interactions in all ferroelectrics.

$LiNbO_3$ and $LiTaO_3$ are called oxygen octahedra ferroelectrics. Six octahedral cages are stacked with shared close-packed planes as shown in **Figure 2a** to form one unit cell with R3c (3m) space (point) group (30–33). Along the $c$ axis of the trigonal structure, the octahedra are filled in the sequence "Li, Nb (or Ta), vacant, Li, Nb (or Ta), vacant . . . ," etc. Two formulae units of $LiNbO_3$ form one unit cell because of staggered oxygens that repeat after two consecutive operations of the $c$-glide symmetry. At room temperature, the trigonal unit cell can be described by hexagonal lattice parameters (34–36). The unit cell directions can also be defined in a right-handed orthogonal notation system ($x$, $y$, $z$), where $z \equiv c$, three equivalent $y$ axes (perpendicular to $z$) lie in the mirror planes $m$, and three equivalent $x$ axes are determined by the unit vector cross-product $\boldsymbol{x} = \boldsymbol{y} \times \boldsymbol{z}$ (see **Figure 2d**). The high-temperature paraelectric phase is trigonal $\bar{3}m$, which transforms to the ferroelectric, trigonal $3m$ phase below the Curie temperature, $T_c$, of ~1198°C for stoichiometric $LiNbO_3$ and ~701°C for stoichiometric $LiTaO_3$ (34). This transition is accompanied by (a) a small displacement of the Nb (Ta) from the center of its octahedron to an asymmetric position along the $c$ axis within the same octahedron and (b) a corresponding motion of the Li from one octahedron to the adjacent vacant octahedron through the intermediate close-packed oxygen plane. The direction of motion of these cations defines the positive end of the spontaneous polarization, $P_s$. Given only two degrees of freedom for this motion, $\pm c$, only two possible domain orientations can exist, $\pm P_s$. Domain reversal from $+P_s$ to $-P_s$ can be considered as a twofold rotation operation of the unit cell about one of the $x$ axes.

### 2.1. Portrait of an Ideal Ferroelectric Wall

Scrymgeour et al. (37) developed the phenomenological GLD theory of trigonal ferroelectric crystals. In the presence of a domain wall, it is convenient to work in a
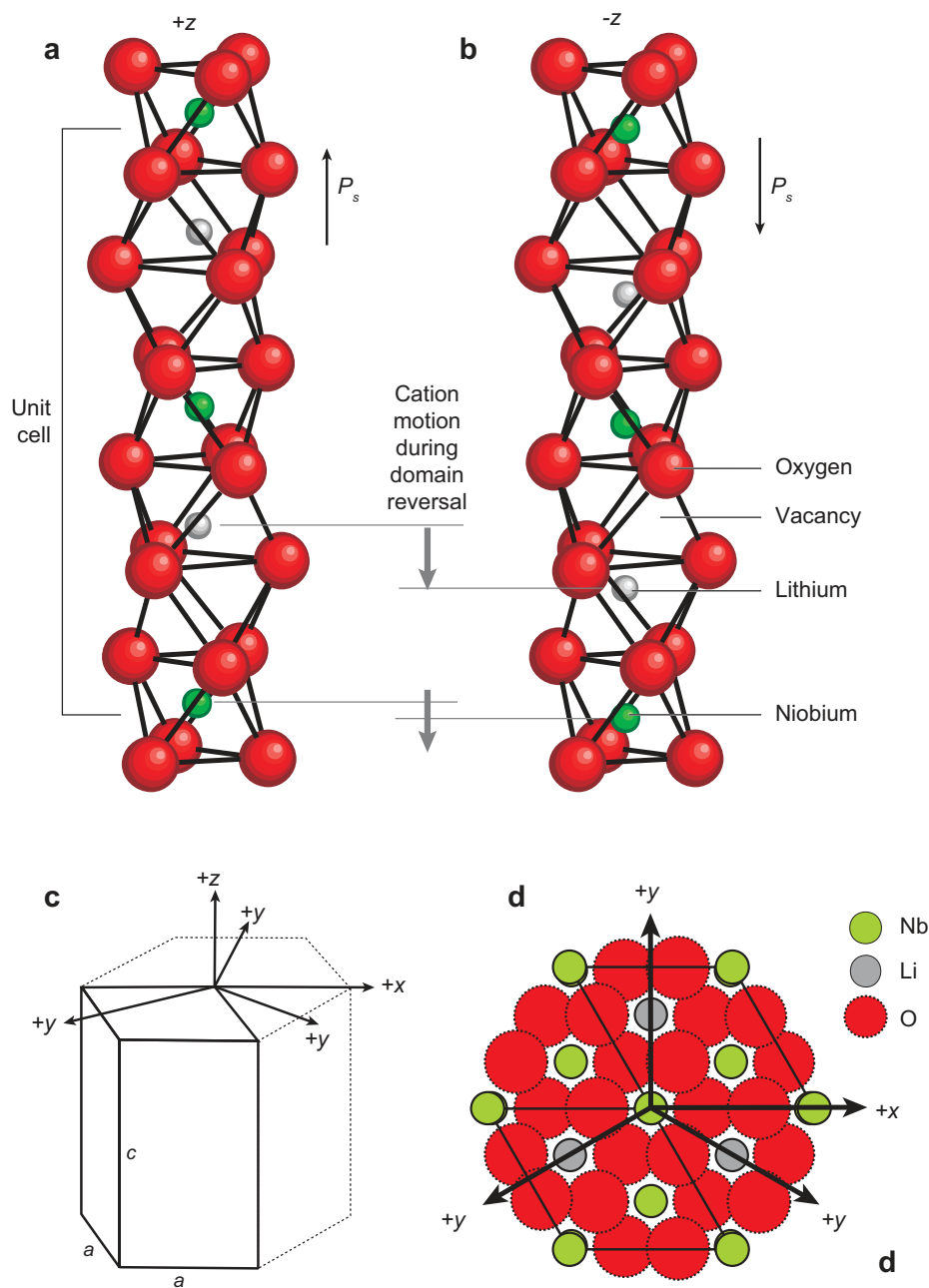
**a** +z

**b** −z

$P_s$

$P_s$

Unit cell

Cation motion during domain reversal

Oxygen

Vacancy

Lithium

Niobium

**c**

+z

+y

+x

+y

+y

c

a

a

**d**

+y

+x

+y

+y

Nb

Li

O

**d**

**Figure 2**

Crystal structure of LiNbO₃ and LiTaO₃. (*a*,*b*) The unit cell for +$P_s$ and −$P_s$ domains. (*c*) A schematic of the relationship between hexagonal (*c*,*a*) and orthogonal (*x*,*y*,*z*) unit cell vectors. (*d*) Schematic of the unit cell along the (0001) zone axis.

right-handed domain wall coordinate system $(x_n, x_t, z)$, where the subscripts $n$ and $t$, respectively, refer to the coordinates normal and parallel to the domain wall and $z$-$x_t$ is the wall plane. The free energy in this coordinate system (Equation 6 in Reference 37) can then be written as a function of angle $\theta$ between the $x$ and $x_n$ coordinate axes; the polarizations $P_z$, $P_n$, and $P_t$; the elastic strains $\varepsilon_n = u_{n,n}$, $\varepsilon_t = u_{t,t}$, $\varepsilon_3 = u_{3,3}$, $\tilde{\varepsilon}_4 = u_{t,3} + u_{3,t}$, $\tilde{\varepsilon}_5 = u_{n,3} + u_{3,n}$, and $\tilde{\varepsilon}_6 = u_{t,n} + u_{n,t}$ (in Voigt's notation, where $u_i$ are the lattice displacements); the electrostrictive coupling energies between the polarization and strain components; and the gradient of polarization, $P_{i,j} = \partial P_i / \partial x_j$, across the domain wall placed in the system. The spontaneous polarization vector, $P_i$, is the primary order parameter in the above expression, whereas the spontaneous strain tensor, $\varepsilon_{ij}$, is a secondary order parameter that depends on $P_i$ (37).

Minimization of the energy under a homogeneous case—i.e., that of no domain walls, uniform polarization ($\partial F / \partial P_i = 0$), and stress-free conditions ($\partial F / \partial \varepsilon_i = \sigma_i = 0$)—results in the following conclusions about a single-domain state: There are no polarizations in the $x$-$y$ plane ($P_n = P_t = 0$) and no shear strains ($\tilde{\varepsilon}_4 = \tilde{\varepsilon}_5 = \tilde{\varepsilon}_6 = 0$). The only spontaneous polarization is in the $z$ direction, $P_z = P_s$, and is given by Equation 11 in Reference 37, in which it is denoted $P_b$. The spontaneous strains are all dilatory and given by $\varepsilon_n = \varepsilon_t = \lambda_1 = \psi_1 P_b^2$ and $\varepsilon_3 = \lambda_2 = \psi_2 P_b^2$. The values of $\lambda_1$ and $\lambda_2$ are, respectively, $\lambda_1 = 6.4 \times 10^{-4}$ and $\lambda_2 = -1.6 \times 10^{-3}$ (for LiTaO$_3$) and $\lambda_1 = 9.36 \times 10^{-4}$ and $\lambda_2 = -4.8 \times 10^{-3}$ (for LiNbO$_3$), indicating that there is a homogeneous tensile strain in the $x$-$y$ plane and a homogeneous compressive strain in the $z$ direction.

Minimizing the free energy with the addition of a domain wall to this system (the inhomogeneous case) and seeking a quasi-one-dimensional solution, in which the polarization and strain fields are functions of only the coordinate normal to the wall (i.e., the coordinate $x_n$), one can rederive the polarization as a kink solution as

$$P_z(x_n) \sim P_s \tanh\left(\frac{x_n}{w_o}\right), \qquad\qquad 1.$$

where $w_o \sim 2\sqrt{g_1/\alpha_1}$ is the domain wall half width (exact expressions are given in Reference 37). This function is plotted in **Figure 3**. Although $\alpha_1 = (2\varepsilon_{33})^{-1}$ values are known experimentally, the values of $g_1$ are determined only by measurement of the wall width over which the polarization, $P$, varies across a wall. Bursill & Lin (15) have measured the domain wall width to have an upper limit of 0.28 nm, using high-resolution TEM images in LiTaO$_3$ (isomorphous to LiNbO$_3$). Taking this as the wall width, $2w_o$, for both materials, one can estimate the upper limit for the gradient term as $3.98 \times 10^{-11}$ Nm$^4$ C$^{-2}$ and $2.53 \times 10^{-11}$ Nm$^4$ C$^{-2}$ for LiNbO$_3$ and LiTaO$_3$, respectively. Bandyopadhyay & Ray (27) have developed a perturbation analysis to probe the stability limits of a kink-like wall (Equation 1) placed in a GLD energy potential that involve only the primary order parameter, $P_z$. The corresponding limits of domain wall width are the upper limit ($x_{o,U} = a/(E_c/\alpha_1 P_s) \sim 50$–$100$ nm) at nondimensional $P_c = P/P_s = 1/\sqrt{3}$ and lower limit ($x_{o,L} = 3a/(2 + E_c/\alpha_1 P_s) \sim 0.74$–$0.77$ nm) at $P_c = 1$ (i.e., $P = P_s$). Here, $a$ is the lattice spacing in nanometers, and $E_c$ is the coercive field required to move domain walls. The estimate of the lower wall "width" of such domain walls for LiNbO$_3$ and LiTaO$_3$ agrees closely with that of Padilla et al.
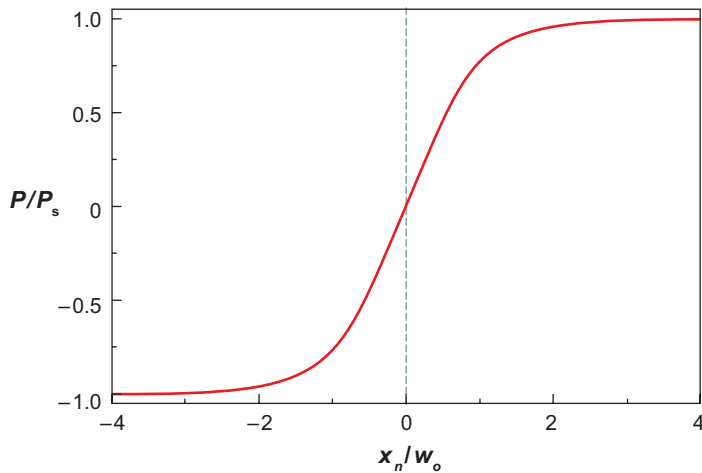
(10). The upper limit is in the range of ∼50–100 nm, which is the width measured by SPM, as discussed below in Section 4.5.

The polarizations in the $x$-$y$ plane, $P_n$ and $P_t$, exist only in the vicinity of a domain wall and disappear away from the wall as plotted across a hypothetical circular domain wall. As **Figure 4a** shows, the $x$-walls have $\vec{P}_{in-plane} = \vec{P}_n$, and in **Figure 4b** the $y$-walls have $\vec{P}_{in-plane} = \vec{P}_t$. This is shown in **Figure 4** for LiTaO$_3$ but is also true
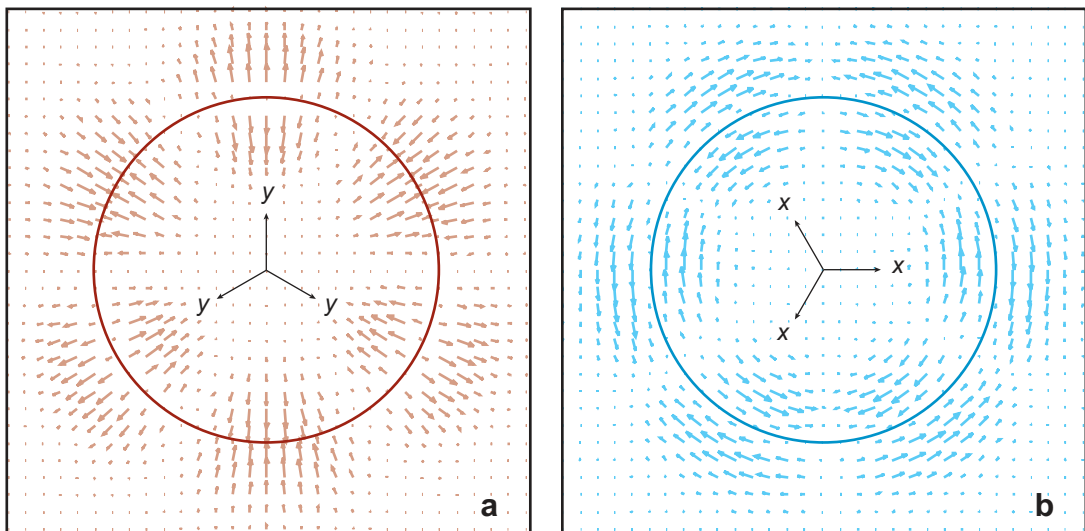


**Figure 4**

(*a*) The normal polarizations, $P_n$, and (*b*) the transverse polarizations, $P_t$, for lithium tantalate (LiTaO$_3$). Lithium niobate (LiNbO$_3$) shows a similar symmetry but with the orientation of the vectors reversed. Reprinted with permission from Reference 37. Copyright 2005 by the American Physical Society.
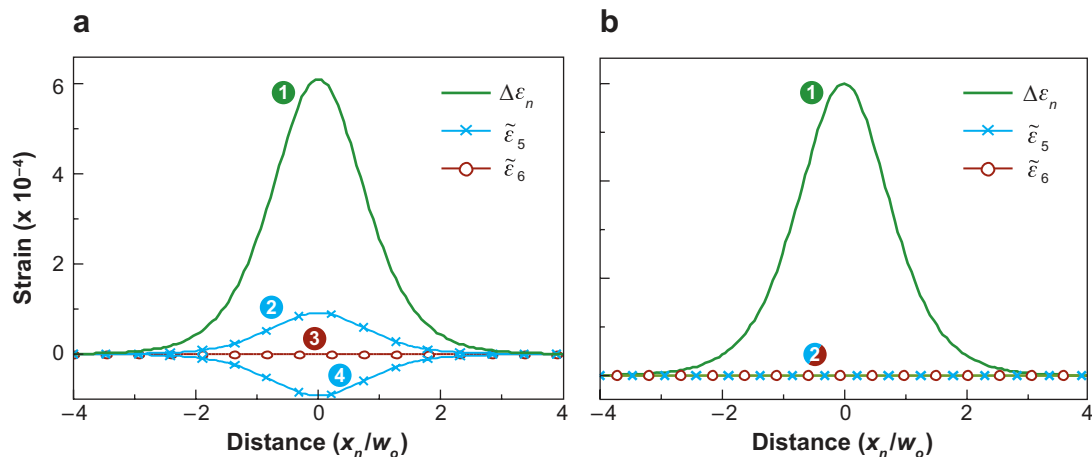
**Figure 5**

The strain in LiNbO$_3$ at $x$- and $y$-walls. (*a*) $x$-walls, for which curve 1 is $\Delta\varepsilon_n$ for $\theta = 30$ and $90°$, curve 2 is $\tilde{\varepsilon}_5$ for $\theta = 90°$, curve 3 is $\tilde{\varepsilon}_5$ for $\theta = 30°$, and curve 4 is $\tilde{\varepsilon}_6$ for $\theta = 30°$ and $90°$. (*b*) $y$-walls, for which curve 1 is $\Delta\varepsilon_n$ for $\theta = 0°$ and $60°$ and curve 2 is $\tilde{\varepsilon}_5$ and $\tilde{\varepsilon}_6$ for $\theta = 0°$ and $60°$. Every tenth point is marked. Reprinted with permission from Reference 37. Copyright 2005 by the American Physical Society.

for LiNbO$_3$. The in-plane polarizations at the $x$-walls are perpendicular to the wall and must therefore be electrically charged walls, leading to higher electrostatic wall energy as compared with $y$-walls. This is a significant feature that defines the domain wall orientations to be $y$-walls in stoichiometric LiNbO$_3$ and LiTaO$_3$ crystals.

**Figure 5** shows the variation of strains as a function of the normalized coordinate $x_n/w_o$ perpendicular to the domain wall in LiNbO$_3$ (37). Although strains vary with wall orientations, the main results are that wall strains are on the order of $10^{-4}$ and are located within $4w_o$ distance in the vicinity of the wall, which for ideal walls is on the order of $\sim$1 nm. Domain wall energy $F_{DW}$ was also numerically evaluated in Reference 37. When the depolarization energy $F_d$ arising from the divergence of in-plane polarizations $P_n$ across a wall is included, the predicted low-energy wall orientations are $y$-walls.

## 2.2. Deviations from Ideality: Nonstoichiometry and Point Defects

LiNbO$_3$ has been studied for 50 years, during which time it has been the subject of multiple reviews and a book (34–36). However, until the 1990s a vast majority of this research focused on congruent composition that is not LiNbO$_3$ but instead Li$_{0.95}$Nb$_{1.01}$O$_3$! The congruent composition on a phase diagram is favored by crystal growers because the melt transforms into a solid at a well-defined temperature without any phase separation. In the past 15 years, and particularly in the past 5 years, crystals of composition very close to that of stoichiometric LiNbO$_3$ and LiTaO$_3$ have been achieved through the development of double crucible Czochralski (DCCZ) (38, 39) and vapor transport equilibration (VTE) methods (40, 41). Recent studies have

shown that the properties of both $LiNbO_3$ and $LiTaO_3$ are extremely sensitive to the $C = Li/(Li+M)$ ratio ($M = $ Nb, Ta), as summarized in **Table 1**. The variation of $C$ from 0.5 (stoichiometric) to 0.485 (congruent) composition causes large shifts in $T_c$ (38, 40, 42); a two-order-of-magnitude increase in coercive field, $E_c$ (40, 42–44), for domain reversal; the creation of large built-in internal fields; the occurrence of domain "backswitching" and stabilization time phenomena; increased domain stabilization time; large changes in photorefraction; and the unexpected creation of optical birefringence, strain, and local electric fields adjacent to the domain walls (45, 46).

Below, we discuss defect models in congruent $LiNbO_3$, which has been studied more extensively. In congruent composition of $LiNbO_3$, Prokhorov & Kuzminov (36) concluded that lithium vacancies $(V_{Li})^+$ and oxygen vacancies $(V_O)^{2+}$ dominate at room temperature, corresponding to a congruent defect structure of $[Li_{0.944}\square_{0.056}]Nb[O_{2.972}\square_{0.028}]$ that we refer to as Model I. However, the density of $LiNbO_3$ increases with increasing lithium deficiency (47), which is incompatible with the oxygen vacancy model. More recently, Schirmer et al. (48) concluded that niobium antisites $(Nb_{Li})^{4+}$ and niobium vacancies $(V_{Nb})^{5-}$ are the dominant point defects and that oxygen vacancy is present at most in negligible concentrations, except when brute force treatments such as high-energy electron irradiation are applied. The chemical formula for this defect model, suggested by Abrahams & Marsh (49), is $[Li_{0.947}Nb_{0.053}][Nb_{0.9528}\square_{0.047}]O_3$, to be referred as Model II. However, Donnerberg et al. (50) showed that the formation of a niobium vacancy was energetically unfavorable as compared with the formation of a lithium vacancy. The third proposed defect model (Model III) involves the presence of niobium antisites $(Nb_{Li})^{4+}$ and lithium vacancies $(V_{Li})^-$ (51). The neutron diffraction studies by Iyi et al. (52) and Zotov et al. (53, 54) support this defect model, with a chemical formula of $[Li_{0.95}\square_{0.04}Nb_{0.01}]NbO_3$. Schirmer et al. (48) point out that the niobium vacancy model and the lithium vacancy model can be reconciled if it is assumed that there are ilmenite-type stacking faults in the regular $LiNbO_3$ crystal structure. However, Ivanova et al. (55) and Yatsenko et al. (56) have interpreted the nuclear magnetic resonance (NMR) spectra in congruent $LiNbO_3$. They concluded that at room temperature, a combination of Models I and III in a ratio of 1.1:1.0 would provide a "rather good qualitative and quantitative agreement with the NMR $^7Li$ spectra." However, these authors asserted that only Model III (with allowance for the mobility of $Li^+$ ions in $LiO_6$ octahedra) can explain the temperature dependence of the experimental NMR $^7Li$ and $^{93}Nb$ spectra from 77 K to 4.2 K. Accordingly, the authors proposed that the structure of a defect complex is composed of a niobium antisite surrounded by three $Li^+$ vacancies in the nearest neighborhood, plus one independent $Li^+$ vacancy along the polar $z$ direction. Yatsenko et al. (57) have also reported that the preliminary analysis of the structural distortions caused by a $Nb_{Li}$ antisite defect reveals a contraction of the nearest three oxygen atoms and a displacement from the $c$ axis of the nearest three $^{93}Nb$ nuclei. This defect complex, composed of one $Nb_{Li}$ with four $V_{Li}$, certainly possesses an electrical dipole moment arising primarily along the $z$ axis from the antisite $Nb_{Li}$ itself as well as from the relative arrangement of $V_{Li}$ around the antisite. This defect model is also supported by X-ray and neutron diffuse scattering of congruent $LiNbO_3$ reported by Zhdanov et al. (58), Ivanov et al. (59), and most recently

**Table 1   A comparison of properties of different compositions of lithium niobate and tantalate crystals**[a,b]

| | Congruent lithium tantalate (CLT) | Near-stoichiometric lithium tantalate (NSLT-CZ) | Stoichiometric lithium tantalate (SLT-VTE) | Congruent lithium niobate (CLN) (24) | Near-stoichiometric lithium niobate (NSLN) (42) |
|---|---|---|---|---|---|
| Growth technique | CZ method | DCCZ method | VTE treatment on CZ–grown CLT | CZ method | DCCZ method |
| Composition, $C$ | 0.485 (38) | 0.499 (42) | ~0.5 | ~0.485 | ~0.498 (42) |
| Curie temperature | 601 ± 2°C (40) | 685 ± 1°C (38) | 701 ± 2.5°C (38) | 1138°C (44) | 1198°C (44) |
| Coercive fields, 296 K | $E_f = 211.55 \pm 2.81$ kV cm$^{-1}$ (42) <br> $E_r = 125.99 \pm 1.65$ kV cm$^{-1}$ (42) | $E_f = 17$ kV cm$^{-1}$ (40) <br> $E_r = 15$ kV cm$^{-1}$ (40) | $E_f = 1.39$–$1.61$ kV cm$^{-1c}$ <br> $E_r = 1.23$–$1.65$ kV cm$^{-1}$ (43) <br> $E_f \sim 1.00$ kV cm$^{-1}$ (43) | $E_f \sim 206.7$ kV cm$^{-1}$ (43) <br> $E_r \sim 168.5$ kV cm$^{-1}$ (43) | $E_f \sim 40.54$ kV cm$^{-1}$ (44) <br> $E_r \sim 33.14$ kV cm$^{-1}$ (42) |
| Internal fields, $E_{int}$ | $E_{int} = 44.28 \pm 2.08$ kV cm$^{-1}$ (34) | $E_{int} = 1.0$ kV cm$^{-1}$ (43) | $E_{int} = 0.065$ kV cm$^{-1}$ (43) | 20–30 kV cm$^{-1}$ (126) | 3.7 kV cm$^{-1}$ (126) |
| UV absorption edge | 275 nm (34) | 260 nm (34) | 256 nm | 316 nm (24) | 308 nm (24) |
| Domain stabilization time | ~1.7 s ($t_{stab,R}$) (24) <br> ~0.1–0.3 s ($t_{stab,V}$) (24) | ~700 ms ($t_{stab,R}$) (40) <br> ~100 ms ($t_{stab,V}$) (44) | <1 ms (both V and R states) if present at all (40) | 10–30 ms ($t_{stab,R}$) <br> 5 ms ($t_{stab,V}$) | ? |
| Polarization, $P_s$ (μC cm$^{-2}$) | 60 ± 3 (43) | 55 ± 3 (20) | 55.2 ± 0.5 (43) | ~75–80$^c$ | ~75–80$^c$ |
| Saturated space charge field, Essc (V cm$^{-1}$) | 1270 ± 300 (127) | ? | 10 ± 8 (127) | ~2000 | ~20,000 |

[a]Abbreviations used: CLT, congruent lithium tantalate; CLN, congruent lithium niobate; DCCZ method, double crucible Czochralski method; VTE, vapor transport equilibrium.
[b]Numbers in parentheses indicate reference numbers. Measurements not referenced below are from this review.
[c]From Hum DS, Route RK, Miller GD, Kondilenko V, Alexandrovski A, et al. (unpublished data).

Zotov et al. (54). These studies conclude that diffuse maxima around the Bragg positions reflect some three-dimensional short-range order of the defect elements and that the homogeneous part of the diffuse planes indicates a random distribution of the defect clusters. Because each niobium antisite requires four lithium vacancies in the neighborhood for overall charge neutrality, Zotov et al. (53, 54) suggest chains such as Li-$Nb_{Li}$-□-Li, Li-□-$Nb_{Li}$-□, Li-□-□-$Nb_{Li}$, etc. as possible combinations.

## 2.3. A Defect Cluster Model

The influence of nonstoichiometry on physical properties can be understood within the framework that point defects arising from such nonstoichiometry are not randomly distributed but organized as defect clusters. These defect clusters can themselves possess a defect polarization $P_D$ that is different from the lattice polarization $P_s$. Arlt & Neumann (60), Lambeck & Jonker (61), and Warren et al. (62) detailed the basic concept of bulk dipolar defect clusters giving rise to domain stabilization and internal fields in ferroelectrics. Kim et al. (24) proposed a plausible model for how the equilibrium states of the defect complexes composed of a niobium antisite surrounded by three $Li^+$ vacancies in the nearest neighborhood, plus one independent $Li^+$ vacancy along the polar $z$ direction, change with domain reversal and lead to internal fields, domain backswitching, and unexpected local wall structure.

**Figure 6** depicts three possible defect states for such a proposed defect cluster in congruent $LiNbO_3$ (or $LiTaO_3$). A stoichiometric $LiNbO_3$ unit cell (**Figure 6a**) is shown in comparison to proposed stable defect states in congruent $LiNbO_3$ (**Figure 6b,d**) at room temperature. These states are achieved by slowly cooling
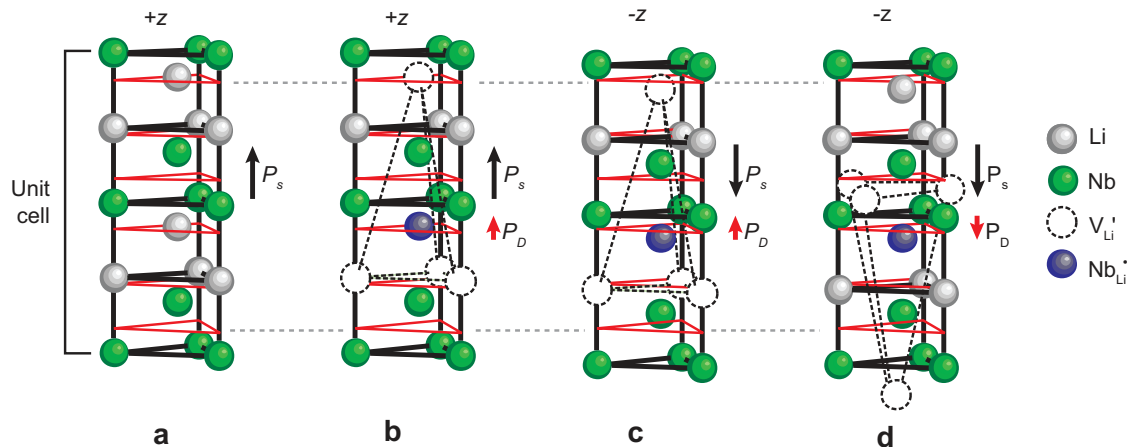


**Figure 6**

Schematics of a possible defect complex involving $Nb_{Li}$ and $V_{Li}'$. (*a*) A stoichiometric crystal with no defects. (*b*) A defect dipole complex in its low-energy configuration. Upon polarization reversal, state *b* becomes state *c*, in which the dipole in *c* is in a frustrated state. State *c* will relax to state *d* after annealing at >150°C, which allows diffusion of $V_{Li}'$. The defect polarization $P_D$ is shown in *b*, *c*, and *d*. The oxygen planes are represented by red triangles. Adapted and modified with permission from Reference 24. Copyright 2001, American Institute of Physics.

the crystal in a single-domain state from high temperature such that the point defects (especially Li vacancies) have enough ionic mobility to form and then freeze into such stable defect clusters at room temperature. [The ionic mobility of Li through the lattice exponentially increases at temperatures above $150°C$, with an activation energy of $\sim 0.66$–$0.72$ eV (34, 63).] In a stable defect state, the defect polarization $P_D$ is assumed to be parallel to the lattice polarization $P_s$. Upon domain reversal at room temperature, domain state (**Figure 6c**) is achieved, which is termed a frustrated defect state. This state is achieved when, upon domain reversal, the niobium antisite defect moves to the neighboring octahedron by the movement of $Nb_{Li}$ through the close-packed oxygen plane. At the same time, the lithium vacancies around the original defect in **Figure 6b** are unable to rearrange around the new antisite position to reach the stable defect state of **Figure 6d** owing to a lack of lithium mobility at room temperature. This frustrated state can be relieved into the stable state of **Figure 6d** after a high-temperature anneal (34, 64).

The actual size of the defect cluster can be more extensive than what is proposed above. Nassau & Lines (65) propose extended stacking fault defects in the structure. Zotov et al. (53, 54), however, restrict the size of such clusters to $\sim 11.4$ Å (approximately four cation sites) to match the correlation length $L_c \sim 13$ Å along the chains calculated from the FWHM of the diffuse X-ray streaks. The average spacing between defect clusters along the chains is estimated to be $\sim 76$ Å. The temperature dependence of diffuse X-ray streaks (54) suggests that at low temperatures the lateral correlations between defect clusters become quite substantial. With increasing temperatures, these correlations decrease, resulting in more random one-dimensional disorder. The changes in the threshold coercive and internal fields with temperature, as reported by Battle et al. (66) and Scrymgeour (67), also point to the breaking up of the three-dimensional clusters with heating followed by reformation of the defect dipole in an energetically favorable orientation upon cooling down to room temperature.

Some important consequences of the above discussion include the following:

1. Point defect clusters that have multiple energy states in relation to the matrix polarization state can form. In the above example, defects can possess two equivalent low-energy states (**Figure 6b,d**) and a frustrated state (**Figure 6c**).

2. The time-temperature dynamics of the reconfiguration of the defect cluster through its multiple energy states can be different from that of the matrix polarization states themselves.

3. In particular, at room temperature, the defect clusters can be in a stable or a frustrated state in relation to the matrix polarization. Specifically, the creation of a $180°$ ferroelectric domain wall in $LiNbO_3$ at room temperature can result in stable defect states (**Figure 6b**) on one side of the wall and frustrated defects (**Figure 6c**) on the other side of the wall. This leads to local wall structures that arise from the interaction of defect clusters with domain walls. Annealing this crystal state results in a reduction in the defect frustration and leads to a change in the wall structure.

With this framework in hand, we next review the experimental observations related to the influence of nonstoichiometry on ferroelectric properties.

# 3. DEFECT INFLUENCE ON MACROSCALE DOMAIN REVERSAL PROCESS

The influence of nonstoichiometry on macroscale domain reversal properties is summarized in **Table 1** and described in detail in a review elsewhere (34). Here we briefly summarize the conclusions. Starting from a single-domain state with stable defect clusters in the crystal (labeled state V with $+P_s$, $+P_D$), the first domain reversal (called forward poling) requires an external electric field of $E_f$ and results in a domain state with frustrated defects (labeled state R with $-P_s$, $+P_D$). Reversal back from R to V state (called reverse poling) requires a different electric field of $E_r$. The difference between the two fields reflects an internal field $E_{int} \sim (E_f - E_r)/2$ and arises directly from defect clusters. As **Table 1** shows, the magnitude of $E_f$ changes linearly with the stoichiometry parameter $C$, ranging from 21 kV mm$^{-1}$ (for congruent samples) to <50 V mm$^{-1}$ (for stoichiometric LiTaO$_3$). The internal fields change linearly with $C$ as well, from ~5 kV mm$^{-1}$ for congruent samples to negligible values for stoichiometric crystals of LiTaO$_3$. Similar trends are seen in LiNbO$_3$ (64). Furthermore, if domains of state R are created by an external electric field in a matrix of domain state V, they require a certain period of time, called the stabilization time, $t_{stab,R}$, for them to be stable after the electric field is removed. If the field is removed earlier, the newly created domains V shrink and disappear, which is called backswitching. A similar stabilization time, $t_{stab,V}$, is required for the domain states V created in a matrix domain of R to be stable. Typically $t_{stab,V} < t_{stab,R}$ for nonstoichiometric compositions. This difference disappears, and in addition the actual magnitude of $t_{stab}$ decreases, as a crystal approaches stoichiometric composition (24).

Upon heating in the temperature range of 25–200°C, interesting changes take place in the crystal; these include decreases in coercive field and internal fields that disappear at approximately 150°C, increases in conductivity (66, 68, 69), and changes in domain morphology (37). In the temperature range of interest (25–200°C), both electronic and ionic conduction mechanisms are active. Conduction occurs when the Nb$_{Li}^{4+}$-based polaron hopping has an activation energy between 0.49–0.9 eV (68–72) for LiNbO$_3$ and between 0.5–0.90 eV for LiTaO$_3$ (73, 74). Ionic conductivity becomes prominent at higher temperatures (~125°C), with an activation energy of ~1.1–1.23 eV (75, 76). The ionic species includes hydrogen diffusion (76–78) and lithium vacancy diffusion (75, 79–81). Extrinsic conduction mechanisms in this material are mainly from iron impurities incorporated into the crystal from the starting raw materials (36, 71).

The domain morphologies are dominated by hexagonal domains, with $y$-walls occurring for all stoichiometries of LiNbO$_3$ and stoichiometric compositions of LiTaO$_3$. This is consistent with the predictions from GLD phenomenological theory described above in Section 2. However, nonstoichiometry does influence the wall orientation in congruent LiTaO$_3$, switching it to $x$-walls. This can arise from additional higher-order gradient coefficients at the wall or a decrease in the energy at the wall that is related to the gradient of in-plane polarization across the wall (37). At higher temperatures, at which the defect clusters break up, the wall orientations appear to revert back to $y$-walls (67).

**a**     $t < 0$ (V state)

**b**     $0 < t < t_{stab,R}$

**c**     $0 < t < t_{stab,R}$

**d**     $t_{stab,R} < t$
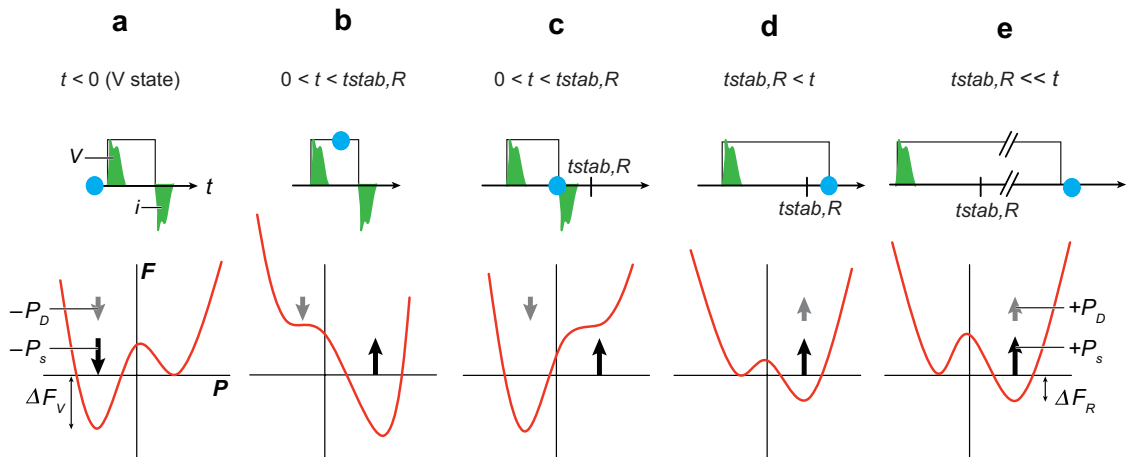
**e**     $t_{stab,R} << t$

**Figure 7**

A schematic describing the process of forward domain reversal from $-P_s$ (V state) to the $+P_s$ (R state) in the presence of the dipolar defect clusters shown in **Figure 6**. Each of the five schematics (*a–e*) shows the voltage pulse $V$ and the transient current $i$ (*top*), followed by the corresponding potential energy well ($F$ versus $P$) (*below*) at the time instant $t$, denoted by a blue circle ($t = 0$ corresponds to the start of the voltage pulse). The positive transient current $i$ indicates a reversal from the V→R states, and negative current indicates backswitching from the R→V states. The lattice polarization ($P_s$), defect polarization ($P_D$), and stabilization time ($t_{stab,R}$) are indicated. For $t > t_{stab,R}$, the defect polarization $P_D$ reorients parallel to the new $P_s$ direction, and no backswitching is observed. Reprinted with permission from Reference 24. Copyright 2001, American Institute of Physics.

Let us now consider these facts from the viewpoint of a defect cluster model proposed in Reference 24. The defect cluster with polarization $P_D$ in **Figure 6** is itself proposed to be composed of a dipole moment, which has two contributions: (*a*) the contribution to the dipole arising only from the $Ta_{Li}$ antisite defect and (*b*) the contribution to the dipole arising from the relative arrangement of the lithium vacancies $V_{Li}$ around a tantalum antisite defect, $Ta_{Li}$. Whereas the first component can switch under electric field at room temperature, the second component does not and requires thermal activation to rearrange. **Figure 7a–e** shows a schematic of the potential energy diagram at room temperature for the lattice with stable (V) and frustrated (R) defect states. In this model, the measured steady state internal field is then given by

$$E_{int}(t) \approx \frac{N(\Delta F_V(t) - \Delta F_R(t))}{4P_s},\qquad 2.$$

where $N$ is the density of defect clusters, $P_s$ is the lattice polarization, and $\Delta F_{V,\ R}$ is the difference in the relative stabilization energy of the V and the R states, respectively, by the defect clusters. The internal field depends linearly on the density of defect clusters, $N$, as is also experimentally observed (43). Heating above ~150°C causes a breakup of these defect clusters, thus resulting in $\Delta F_{V,\ R} = 0$. Cooling results in a rearrangement of lithium vacancies to reform stable defect clusters and thus recover the low-energy domain states V. As an example, for congruent $LiTaO_3$,

the coercive fields are $E_{c,f} \sim 21$ kV mm$^{-1}$ and $E_{c,r} \sim 11$ kV mm$^{-1}$, resulting in a measured internal field of $E_{int} \sim 5$ kV mm$^{-1}$. For stoichiometric LiTaO$_3$, $E_{c,f} \sim E_{c,r} \sim 50$ V mm$^{-1}$, and hence $E_{int} \sim 0$. If we write the coercive field as $E_c$(congruent) $= E_c$(stoichiometric) $\pm E_D$, where $E_D$ is termed an equivalent defect field, then $E_{d,V} \sim 20.95$ kV mm$^{-1}$ and $E_{d,R} \sim 10.95$ kV mm$^{-1}$, which indicates that the coercive fields in congruent compositions are dominated by defect fields. (These defect fields, $2E_{D,V}P_s$ and $2E_{D,R}P_s$, can be considered equivalents to the corresponding energy differences $N\Delta F_V$ and $N\Delta F_R$, respectively, in Equation 2.)

The phenomena of domain backswitching and stabilization times come from the time dependence of these defect fields, as described in detail in Reference 24. Consider forward domain reversal from states V to R. Immediately after the domain reversal, the defect field is still in its original orientation (parallel to the V state) and hence destabilizes the new state R. The instantaneous coercive field for this state R is therefore $E_c$(stoichiometric) $- E_{D,V} \sim -20.95$ kV mm$^{-1}$. This large negative coercive field essentially makes the new R state unstable unless an external field that is greater than this value is maintained, stabilizing the R state. If such an external field is maintained, the defect field slowly reverses sign with time from a value of $-E_{D,V} \sim -20.95$ kV mm$^{-1}$ to a value of $+E_{D,R} \sim +10.95$ kV mm$^{-1}$. The plus and minus signs here correspond to whether the defect field is, respectively, parallel or antiparallel to the matrix polarization state (in this example, the R state). The new defect field of $+E_{D,R}$ in the R state stabilizes this domain state. The time required for the defect field to relax from $-E_{D,V}$ to a value of $< -E_c$(stoichiometric) is called the stabilization time. If the external field is removed after this time, the defect field does not destabilize the new domain state R, and no backswitching occurs. The defect fields $E_{D,V}$ and $E_{D,R}$ in the stable and frustrated states, respectively, reflect the influence of stable and frustrated defect cluster states. The internal field, $E_{int}$, essentially arises from the difference in these defect fields, i.e., $E_{int} \sim (E_{D,V} - E_{D,R})/2 \sim 5$ kV mm$^{-1}$, which is equivalent to Equation 2 above and a more meaningful definition than the $E_{int} \sim (E_{c,f} - E_{c,r})/2$ that was stated above.

Macroscale domain nucleation and growth have been studied in real time via electro-optic imaging microscopy (34, 82). Interestingly, as **Figure 8** shows, in congruent compositions of LiNbO$_3$ and LiTaO$_3$ with domain walls, local but pinned domain wall motion can occur on a micrometer scale under electric fields that are well below the coercive field of 21 kV mm$^{-1}$ (83, 84). These studies therefore suggest that the effect of the nonstoichiometric defect clusters is to pin domain wall motion. The coercive fields can then be considered as the fields at which a pinning-depinning transition occurs.

## 4. DEFECT INFLUENCE ON THE LOCAL STRUCTURE OF DOMAIN WALLS

### 4.1. Index Contrast at a Domain Wall

For uniaxial materials in question, the two refractive indices of interest are the extraordinary index, $n_e$ (along the $c$ axis), and the ordinary index, $n_o$ (perpendicular to
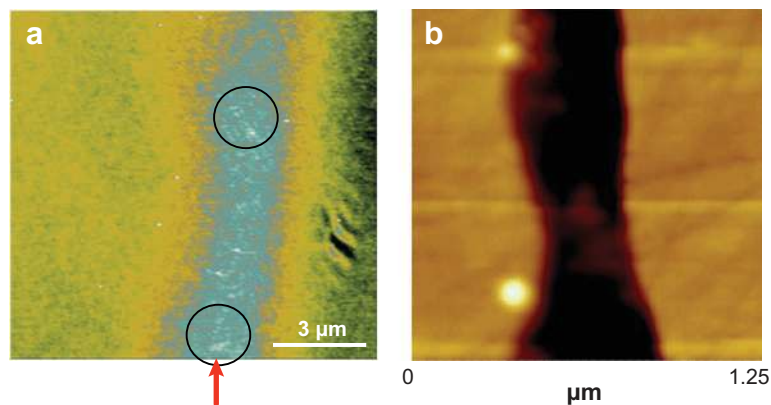
**Figure 8**

Domain wall pinning and bowing under an external field of $+2 \text{ kV mm}^{-1}$ in congruent
$\text{LiNbO}_3$. (*a*) Near-field scanning optical microscopy (NSOM) image of the $+z$ surface of
$\text{LiNbO}_3$. Pinning sites are indicated by circles. The red arrow indicates the center of the wall.
Reprinted with permission from Reference 83. Copyright 1999 by the American Physical
Society. (*b*) Atomic force microscopy images on the $+z$ surface after polishing away 7 μm and
chemical etching (125). Reprinted with permission from Reference 84. Copyright 2006,
American Institute of Physics.

the *c* axis). The refractive index, $n_{ij}$, is a centrosymmetric property and is the same
between two domains related by inversion symmetry operation. The 180° domains
should be optically indistinguishable.

The presence of nonstoichiometry in the crystal, however, changes the situation
completely. Optical microscopy reveals an unexpected index contrast across antipar-
allel domain walls in congruent $\text{LiNbO}_3$ and $\text{LiTaO}_3$ single crystals (19, 34, 85).
With randomly polarized white light optical microscopy, the walls show a weak scat-
tering and thus appear darker than the matrix in transmission. By placing the sample
between two cross-polarizers, one can also observe birefringence at the wall. Using
cross-polarized near-field scanning optical microscopy (NSOM), Yang et al. (83) have
reported estimates for an optical birefringence near the domain wall ($B = |n_{o,\perp} - n_{o,||}| \sim$
$1.2 \times 10^{-4}$), where subscripts $\perp$ and $||$ correspond to ordinary index, $n_o$, perpendic-
ular and parallel to a domain wall. In addition, Kim & Gopalan (19) and Kim (86)
show that a more localized index contrast at the wall location itself exists, as described
next.

**Figure 9** shows NSOM images (transmission-collection mode) of 180° domain
walls in $\text{LiNbO}_3$. In this geometry, light is incident from far-field normal to a z-cut
sample, and the transmitted light through the sample is collected by a 50-nm near-
field tip aperture. The domain state R is always brighter than domain state V. This
can be confirmed by creating either hexagonal domains of state R inside a matrix
domain of state V (**Figure 9a**) or hexagonal domains of state V embedded in a matrix
of domain state R (**Figure 9b**). The contrast reverses in these two samples. Recalling
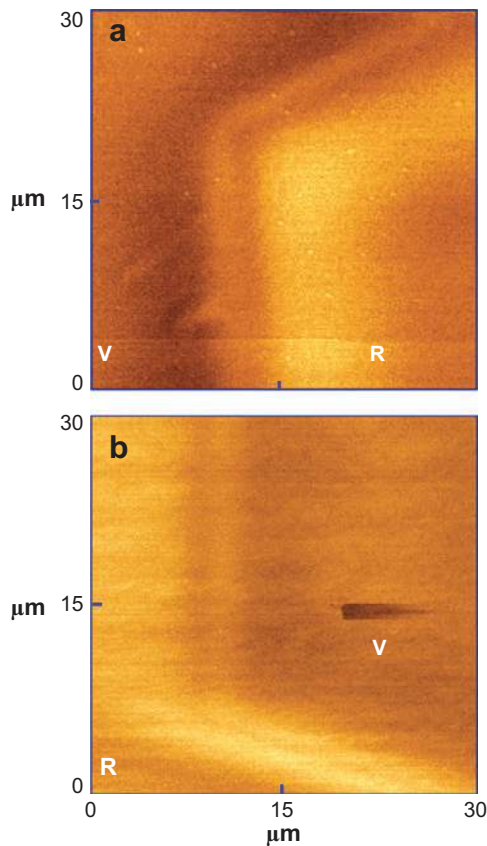that state R has frustrated defect clusters and state V has stable defect clusters, we

conclude that frustration of defect clusters results in an increase in the ordinary refractive index. In addition, **Figure 9** shows a dark rib-like line contrast across the domain wall. One can further confirm that this contrast is nonstoichiometry related by annealing this crystal above 150°C, followed by cooling back. This results in a near-complete loss of the optical contrast across the wall. The optical contrast also disappears in stoichiometric composition of these crystals.

In comparing experimental and simulated NSOM images of domain walls, the approach adopted by Kim & Gopalan (19) is first to make an educated guess for the refractive index profile across the domain wall. Using this profile as a starting point, Kim (86) developed a hybrid code that seamlessly tailors together finite difference time domain (FDTD) and beam propagation method (BPM) techniques for simulating these images.

**Figure 10** shows the refined index distribution model and the resultant BPM simulation of the light intensity after the light has traveled through a 500-μm-thick crystal with a single domain wall. The refined index profile consists of a wide step index profile of index change, $\Delta n_o = n_{o,R} - n_{o,V} \sim 1 \times 10^{-3}$, with a step transition range of $\sim$20 μm across the wall. The ordinary refractive index is higher

**Figure 10**

(*a*) Index profile (*red line*) and the intensity of light (*gray line*) emerging after propagation through a domain wall in a 500-μm-thick crystal. (*b*) Comparison of the experimental (denoted by *A*, *B*, and *C*) and modeling (*solid thick line*) profiles of the intensity variations across a wall in congruent LiNbO$_3$. Inset shows **Figure 9*a***; the three lines indicate the positions of the three experimental line profiles (*black*, *green*, and *blue*) shown in the main plot. Reprinted from Reference 19, with permission from Elsevier.
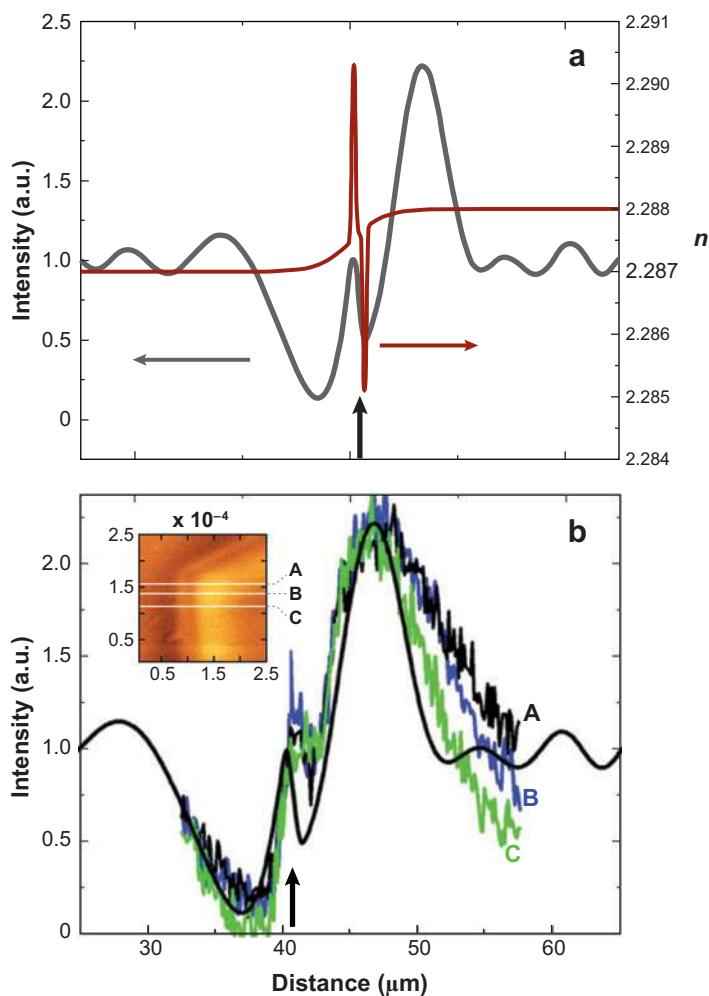


$(n_{o,R} \sim 2.288)$ in the domain-inverted region (R) as compared with the index of the matrix domain $(n_{o,V} \sim 2.287)$ in the virgin state (V). This essentially explains why the domain-inverted region is brighter than the matrix domain. In addition, a sharp index profile kink of $\Delta n_o \sim \pm 3 \times 10^{-3}$ and localized at the center of the wall over a width $\leq 2$ μm (upper limit) is also assumed, as shown in **Figure 10*a***. **Figure 10*b*** shows three experimental line scans across the domain wall in LiNbO$_3$ with the numerically simulated fit. The agreement between the two is excellent.

However, this agreement is not sufficient to determine the uniqueness of the refined index profile in **Figure 10*a***, and additional illumination-mode imaging is required. In illumination-mode NSOM, the small 40-nm aperture fiber tip becomes the light source and scans the desired sample area. Most of this diverging beam is again collected by an infinity-corrected microscopy objective lens. **Figure 11*a*** shows
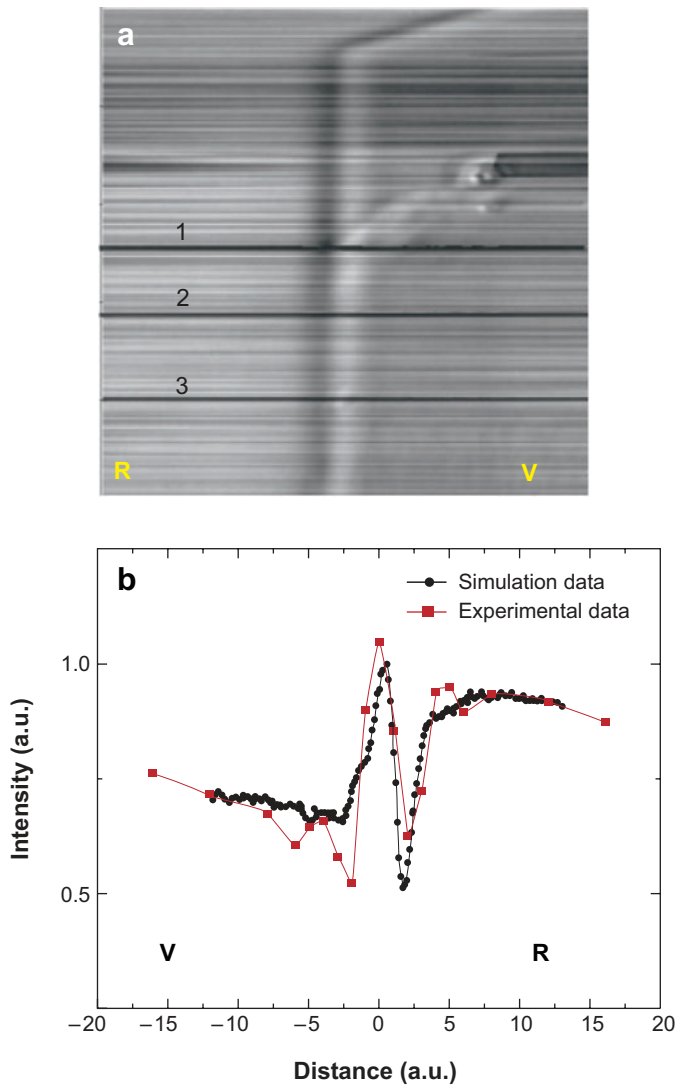
the LiNbO$_3$ experimental NSOM illumination-collection images with the fiber tip slightly out of the focus of the collection objective lens. The defocusing is done by moving the collection objective toward the detector, which helps improve the image contrast as compared with the exact focus case. The same index distribution shown in **Figure 10*a*** is used in the illumination geometry to regenerate the NSOM contrast. **Figure 11*b*** shows such a numerically calculated line scan image for the defocus case, which closely resembles the experimental line scan. The uniqueness of the index profile extracted from the transmission-collection mode is thus confirmed.

One can calculate electric fields at the wall from the optical measurements. The birefringence at $x$-walls in congruent LiTaO$_3$ is proportional to (83)

$$\frac{2B}{n_o^3} = \{2p_{14}d_{15} - 2d_{22}(p_{11} - p_{12}) - 2r_{22}\}E_2 + \{(p_{11} - p_{12})(\gamma_{12} - \gamma_{11})$$

$$- 2\gamma_{14}p_{14} + (K_{12} - K_{11})\} \left(E_2^2 - E_1^2\right) + \{4(p_{11} - p_{12})\gamma_{41} + 4p_{14}\gamma_{44} + 4K_{14}\}E_2E_3. \quad 3.$$

Here, directions 1 and 2 are parallel (perpendicular) to the domain wall, whereas $x_3$ is normal to the plane of the figure. $p_{ij}$ are photoelastic constants, $r_{ij}$ are linear electro-optic constants, $E_k$ is the electric field, and $K_{ilm}$ are the quadratic electro-optic constants. In Equation 2, strains $\varepsilon_j$ are replaced by $\varepsilon_j = d_{mj}E_m + \gamma_{ilj}E_iE_l$, where $d_{mj}$ are the piezoelectric constants and $g_{ilj}$ are the electrostrictive constants. The bulk material constants can be used owing to the small value of strain (87). If we substitute the measured birefringence of $1.2 \times 10^{-4}$ and neglect the electrostrictive and quadratic electro-optic terms in Equation 2 (contribution: 10%), the calculated internal electric field across the domain wall, $E_2$, is 20 kV mm$^{-1}$. We can get an alternate estimate as follows: If we apply a uniform external electric field, $E_{3,ext}$, across the crystal in a direction opposite to the V state, the net electric field $E_3$ in Equation 2 is $E_3 = E_{3,int} + E_{3,ext}$. The experimental variation of birefringence in congruent LiTaO$_3$ as a function of external electric field (83) is given by $B = 1.2 \times 10^{-4} + 10^{-11} E_{3,ext}$ (V m$^{-1}$).

From Equation 3, the slope of $B$ versus $E_3$ is proportional to photoelastic and electro-optic coefficients as well as $E_2$. Taking physical constants (87) of $K_{14} = 0.2$–$2 \times 10^{-20}$ m$^2$ V$^{-2}$, we calculate the electric field $E_2 \sim 20$–200 kV mm$^{-1}$. The lower value of $E_2 \sim 20$ kV mm$^{-1}$ agrees with the above estimate from birefringence. Furthermore, by extrapolating the measurement to zero birefringence ($B = 0$), one can calculate an offset electric field of $E_{3,int} = 12$ kV mm$^{-1}$. This is the equivalent intrinsic electric field across the two domains V and R and points in the same direction as the V state (opposite to the R state). Note that this field is approximately equal to $E_{D,V} - E_{D,R} \sim 10$ kV mm$^{-1}$ and indicates that a large contribution of the field at the wall arises from the energetic difference between the R and V domain states.

## 4.2. Long-Range Strains at a Domain Wall

Kim et al. (20) and Jach et al. (21) demonstrated that owing to its nonstoichiometry the local strain near an antiparallel domain wall in congruent LiNbO$_3$ is spatially extended over many microns. Through the use of highly collimated X rays (divergence: 1.4 μrad), a series of (00.12) Bragg reflection images is shown in **Figure 12** across the Bragg peak.

For the (00.12) and (00.$\overline{12}$) reflections at 8.5 keV, the difference in structure factor is only ~9%. The remaining contrast between domains and their surrounding matrix is the result of surface distortions and changes in the lattice spacing. The wall types 1, 2, 5, and 6 (see labels in **Figure 12a**) in every hexagonal domain are not parallel to the incidence plane and show an enhanced contrast over a wide region (~10 μm wide) of associated strain. The wall types 3 and 4, however, are parallel to the incidence plane and show the least contrast. This contrast phenomenon reveals itself more clearly on moving away from the Bragg peak and reverses contrast between **Figures 12a** and **c**,
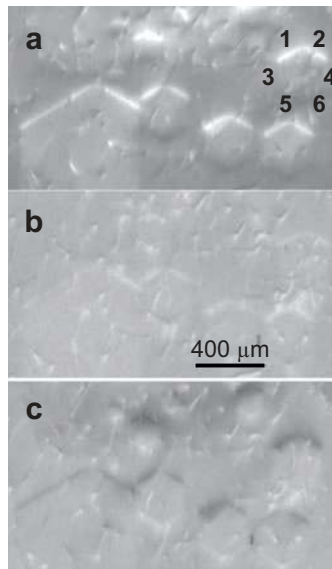
**Figure 12**

Bragg topograph of domains in congruent LiNbO$_3$ crystal on the (00.12) rocking curve
(*a*) –0.003° from the Bragg peak, (*b*) at the Bragg peak, and (*c*) at +0.003° from the Bragg peak.
Incidence plane is along the vertical edge of the images.

hence suggesting a curvature of lattice planes in the wall region from one domain to
the other that can be described by the strain component *dz/du*, where *u* is the outward
normal to a wall (pointing into the matrix domain) and *z* is the coordinate along the
direction of ferroelectric polarization (normal to the image plane in **Figure 12**).
Such a wall curvature would be expected to cause a deviation of the incidence angle,
$\theta$, from $\theta_B$ and influence the Bragg diffraction condition most strongly when the
wall is perpendicular to the incidence plane and least when the wall is parallel to the
incidence plane. This is consistent with the experimental observations in **Figure 12**.
Knowing the difference between the Bragg angles between **Figures 12*a*** and ***c***, we
therefore estimate that the $\Delta\theta_B(1, 2) = \theta_B(1, 2) - \theta_B(\text{center}) = -0.0030° \pm 0.0015°$
and similarly that $\Delta\theta_B(5, 6) = +0.0030° \pm 0.0015°$. In LiNbO$_3$, the domain walls are
parallel to the crystallographic *y* axis ([1$\bar{1}$00] direction), and therefore the observed
shear strain is $\varepsilon_{zx}$. Therefore, $\varepsilon_{zx}(1, 2) \approx -6 \times 10^{-5} \pm 2.6 \times 10^{-5}$ and $\varepsilon_{zx}(5, 6) \approx +6 \times 10^{-5} \pm 2.6 \times 10^{-5}$.

In addition to the Bragg geometry measurements described above, Laue geometry
was used in anomalous transmission mode (see **Figure 13**). In **Figure 13*a***, the interior
of the hexagonal domain (state R) has a darker contrast than the matrix domain (state
V); in **Figure 13*d***, this contrast is reversed. One can therefore estimate that the Bragg
angle for the (3,0,.,0) reflection is smaller in domain state R than in state V by an
upper bound of <0.006°. Through the use of the simple relation $\Delta d/d = -cot\theta \Delta\theta$, the
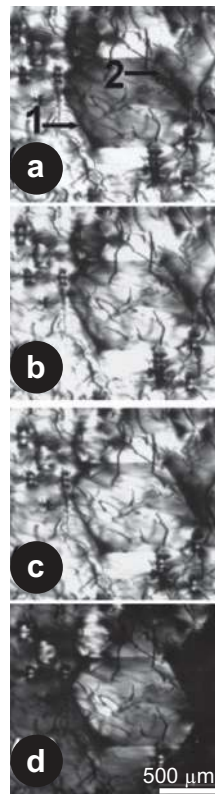stain difference between the two domains is roughly estimated to be $\varepsilon_{yy} < 2.4 \times 10^{-4}$.

**Figure 13**

Rocking image of a domain in congruent LiNbO$_3$ in Laue geometry for (3,0,0) symmetric transmission. Incident angles are (*a*) 22.151°, (*b*) 22.149°, (*c*) 22.147°, and (*d*) 22.145°, respectively (86). The arrows and labels in subpanel *a* can be ignored for the purposes of this review.

Because of the negative sign, the domain state R has a higher lattice spacing $d(3,0,.,0)$ than the outside matrix domain V.

## 4.3. Local Electric Fields Across a Domain Wall

Dierolf & Sandmann (88) have introduced the concept of designer defects, in which they deliberately introduce defects (e.g., Er or other rare-earth ions) into the sample. These defects have strong emission signals and are sensitive to their environment (i.e., local electric fields, defect configuration). This concept allows the influence of defects on ferroelectric domain walls to be studied with high spatial resolution and with sensitivity to specific defect configurations. At low concentrations ($<10^{-2}$ mol%), the rare-earth dopants act as passive probes of local electric fields and do not influence the physical properties of the LiNbO$_3$ or LiTaO$_3$ crystals.

The Er ion in LiNbO$_3$ occupies mainly the Li site (89) and possesses a large number of excitation/emission transitions that result in complicated spectra, particularly
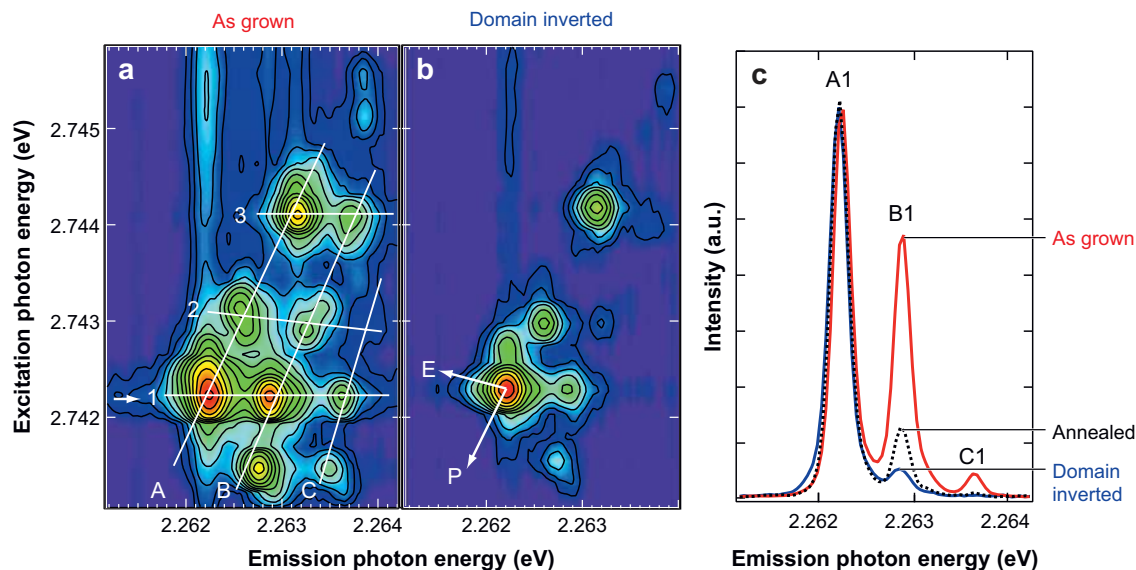
**As grown**  **Domain inverted**

**Figure 14**

Image and contour plot of CEES data taken at 4 K for single excitation and emission
transitions of $Er^{3+}$ in stoichiometric $LiNbO_3$ (*a*) before and (*b*) after domain inversion.
(*c*) Individual spectra taken at the excitation energy indicated by white arrow in *a*. In *a* the
white lines illustrate the hierarchy of sites. The arrows in *b* indicate the shifts that are observed
under the application of an electric field (E) and hydrostatic pressure (P). In the depicted
spectral range, only one excitation and emission transition is expected. Therefore, only one
peak should appear per site, and the different sites can immediately be identified as the
different mountains, labeled as L# with L = A, B, C and # = 1, 2, 3. The differences among
these sites are due to the perturbation by different charge-compensating defects. The main
site in near-stoichiometric $LiNbO_3$, namely A1, is assigned to a center that does not have any
local charge compensations. All others have a local charge compensation along the *z* axis (B1,
C1) or off the axis (A2, A3), or both (B2, B3, C2, C3..). Reprinted with permission from
Reference 90. Copyright 2003, American Institute of Physics.

in the presence of multiple sites. This wealth of information can be unraveled and
exploited via the use of an experimental technique, combined excitation-emission
spectroscopy (CEES) (90), that allows one to obtain spectral fingerprints. **Figure 14**
shows an excerpt of the resulting two-dimensional emission intensity map.

The use of CEES under the application of electric fields yields site-selective Stark
shifts (22; see **Figure 14**) that can be used to calibrate the probe to "measure" intrinsic
electric fields. For the transition depicted in **Figure 14**, the emission shift is $4 \times 10^{-3}$ meV $\pm 1.5 \times 10^{-3}$ meV per kV mm$^{-1}$ of applied field.

On this basis, Dierolf and his group (90) have studied the changes that occur
under domain inversion. **Figure 14** shows CEES data before (V state) and after
(R state) a domain inversion performed at room temperature in nearly stoichiometric
$LiNbO_3$ material. They observe that, whereas the emission strength of the center
type A remains virtually unchanged, the strength of emission from center of types

B and C is reduced. All emission lines are shifted slightly to lower energy. After a subsequent domain inversion back to the initial direction of the ferroelectric axis, these changes are almost completely reversed. Annealing the samples ($T = 250^{\circ}$C, 5 h) at temperatures for which the Li ion is mobile also yields changes in the relative emission intensities of the sites of types B and C. Annealing of as-grown (V state) and domain-inverted (R state) samples results in the same emission spectra at room temperature. These observations suggest that the thermal equilibrium of the defect configuration is perturbed by the domain inversion but can be reestablished by annealing.

To understand the origin of the observed changes, we need to recall that the domain inversion process has been performed at temperatures at which the charge-compensating defects cannot rearrange in their location relative to the ferroelectric axis and the $Er^{3+}$ position. The $Er^{3+}$ ion, however, will rearrange in a manner similar to the Li ions it replaces. As described above, this leads to frustrated defect dipoles, both for intrinsic defect dipoles and for those that include an Er ion.

These spectroscopy studies provide the tools to "measure" the intrinsic electric field changes and frustrated defect configuration across a domain wall. In such studies, a confocal luminescence microscope is used to measure spectra with a spatial reso-lution of approximately 500 nm. Results exist so far only for the near-stoichiometric $LiNbO_3$ samples (2 kV mm$^{-1}$ coercive field) with Er concentration of $10^{-2}$ mol% (see **Figure 15**). In these experiments, freshly prepared domain-inverted regions (state R) were used, and line scans across a domain wall were collected. The same experiment was repeated after the sample had been annealed for 5 h at $T = 250^{\circ}$C. The effect of intrinsic defect dipoles can be observed by the shift of peak A1 that originates from Er ions that have no local charge compensation and exhibit a spectral shift owing to the intrinsic fields created by frustrated defects. We see the following easily resolved spatial features:

1.  A 4-μm-wide peak at the center of the domain wall region is present before and after annealing. The peak represents a maximum shift of 0.02 meV that corresponds to a change in the electric field of $5 \pm 2$ kV mm$^{-1}$ that is expe-rienced by the Er-ion probe. This peak at the wall may come from very local distortions at the wall location. Because the peak remains after annealing, this effect most likely is not due to nonstoichiometric defect clusters but rather to the presence of Er in the wall region where a polarization gradient exists. This may lead to a difference in the off-center position of the Er ion away from the value determined for the bulk material (89). In this environment, the Er ion "measures" a different field. Another possibility is that any local tilts in the wall also induce polarization charges and fields that are symmetric across the wall and give rise to a symmetric peak, as seen for Er at the wall.

2.  The step transition of the peak positions across the domain wall occurs within ∼22 μm. This effect is reduced after annealing; before annealing, a shift of 0.04 meV and a corresponding change in the local field of $\Delta E \sim 11.5 \pm 4.5$ kV mm$^{-1}$ are observed. Although a similar measurement currently is not available for congruent composition, we assume that this is the lower limit for the domain wall fields. After annealing, these values are 0.015 meV and
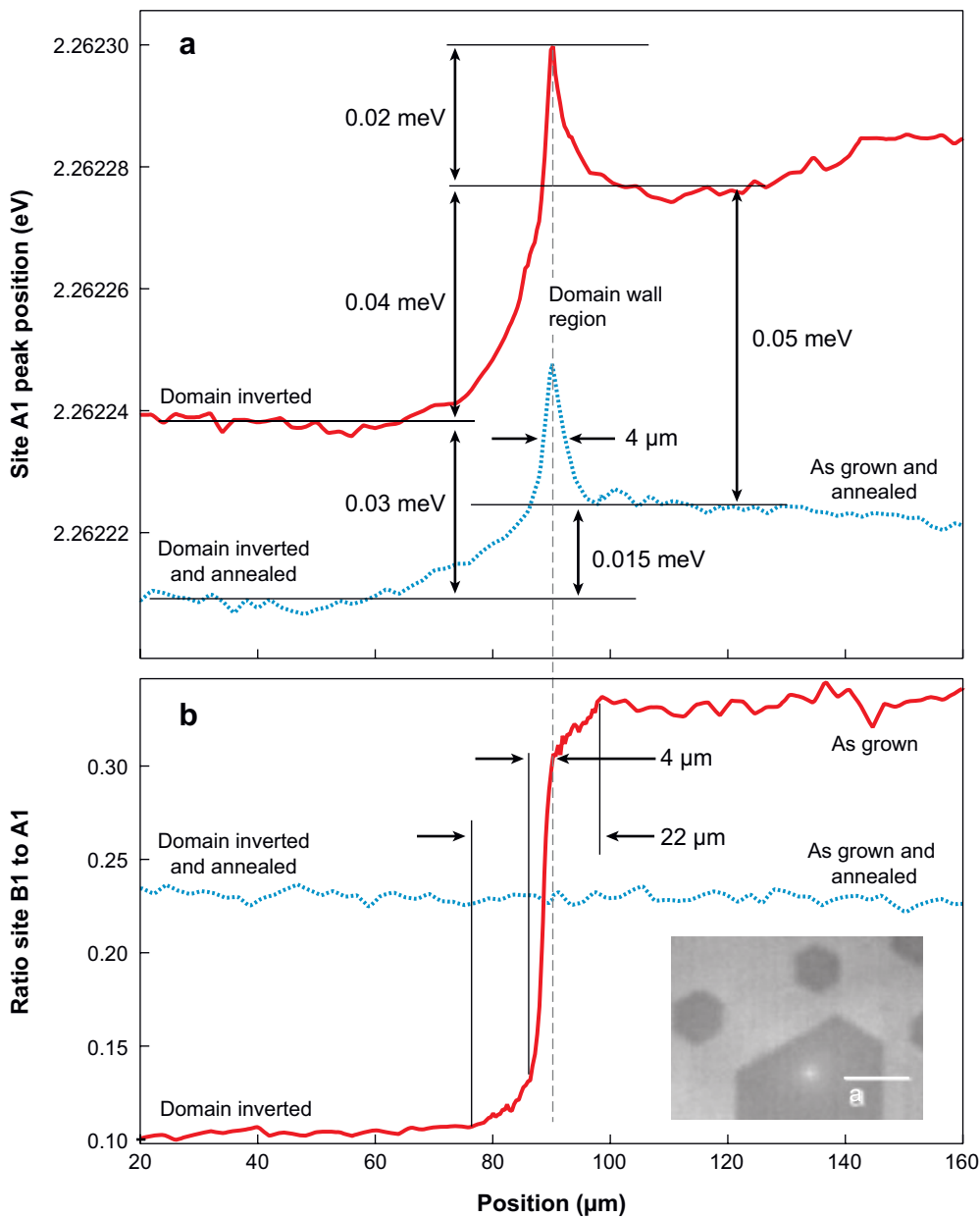
**Figure 15**

Evaluated emission data for a scan over a domain wall region (see *inset*) for a nearly
stoichiometric sample before and after annealing (5 h, 250°C). (*a*) Spectral position of the
emission from site A1 (see **Figure 14**). (*b*) Intensity ratio of main site A1 and satellite peak B1.
The data were collected at 4 K. From Reference 92, with permission from Wiley & Sons.

$\Delta E \sim 4.35 \pm 1.65$ kV mm$^{-1}$, respectively, indicating that the sample has not reached a new thermal equilibrium for the annealing conditions used in this experiment. Such a step change in peak position across the wall cannot arise from local wall tilts, which are expected to have a symmetric response across the wall. It could arise, however, from an uneven charge accumulation across the domain wall.

In the ratio of the emission from A1 and B1, we can observe the behavior of the Er ions that participate in defect cluster formation. We found a short-range component over $\sim 4$ μm and another one with an extent of $\sim 22$ μm. Both disappear completely after annealing, indicating that the rearrangement of defects clusters is different for the A- and B-type Er sites considered here.

The domain wall imaging technique based on rare-earth probes can be extended to allow in-situ observation of a moving domain wall. In this mode of operation, the point of observation is kept constant, and the growth of an existing domain nucleus is induced by the application of an electric field. Spectra are recorded in rapid fashion (100 spectra s$^{-1}$) while a domain wall is moving through the spot of observation. The velocity of domain wall motion can be controlled by the applied field and is determined independently via regular microscope imaging with a CCD camera. For these room temperature measurements, the spectra of individual sites are no longer resolved, but the ratio of site A and B is still reflected in a shift of the unresolved emission band. **Figure 16** shows the result for a growing domain wall for the sequence shown on the bottom panel of the figure. The measurements were performed for several of the sequences with different wall velocities. The domain wall regions were expanded and reached approximately 16 μm in width for a speed of 25 μm s$^{-1}$, up from 4 μm in the static case. This is a significant result because it suggests that adjacent domain walls may interact over long distances.

The transmitted light that detects phase differences due to local strains in the sample was measured simultaneously with the Er emission. This direct comparison shows that the two methods probe changes on somewhat different length scales and clearly different spatial details. Whereas the transmission shows increased and decreased signals, indicating compressive and tensile regions, the Er emission shows as a function of time the same type of dependence as in the static case.

## 4.4. Changes in Phonon Spectra Across a Domain Wall

The imaging technique described above requires a suitable dopant ion and hence is not applicable for undoped samples. In contrast, Raman scattering is intrinsic and

───────────────────────────────────────────────────────────────── →

**Figure 16**

Evaluated emission data recorded at the spot as a function of time while a domain wall is moving though it (velocity: 25 μm s$^{-1}$). (*Top*) Relative emission peak position and intensity of transmitted light. (*Bottom*) Time sequence from camera observing the moving domain wall. The white dots indicate the point of observation. From Reference 92, with permission from Wiley & Sons.
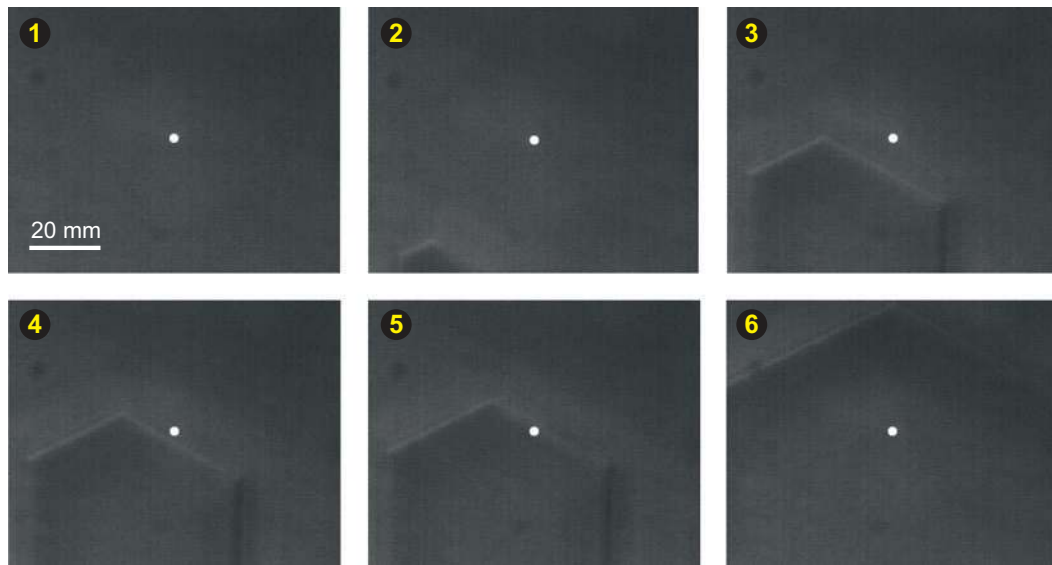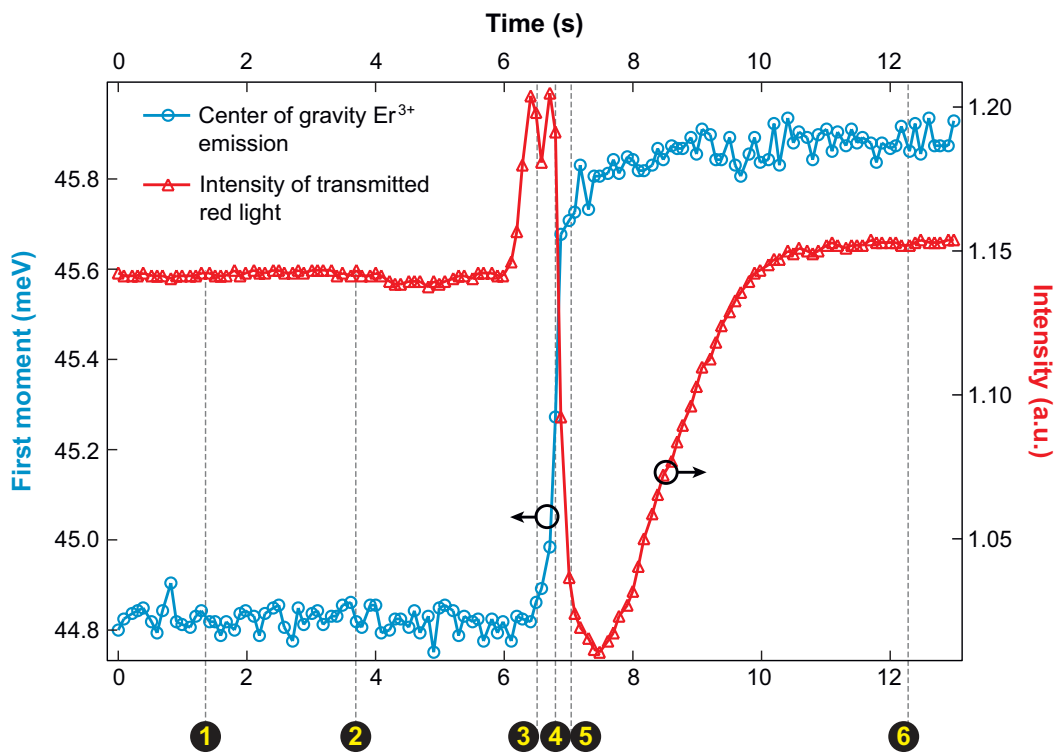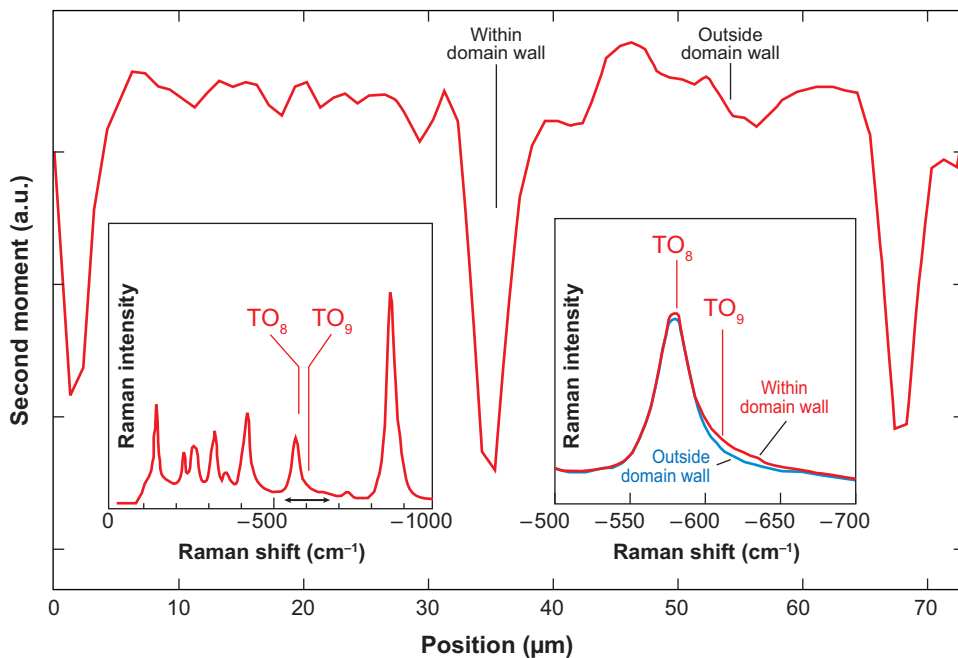
**Figure 17**

The second moment of the Stokes Raman spectrum for a line scan across domain boundaries. The left inset shows the complete Raman spectrum. The arrow indicates the spectral region used for calculating the second moment. The right inset shows the Raman spectra at approximately 600 cm$^{-1}$ for regions within and outside the domain wall. The positions that these spectra have been taken are indicated. From Reference 93, with kind permission of Springer Science and Business Media.

offers information about the local structure as well. For LiNbO$_3$ and LiTaO$_3$ crystals, which belong to the C$^6_{3v}$ space group, there are four $A_1$ and nine $E$ Raman modes expected. Here we describe confocal Raman microscopy studies of z-cut LiNbO$_3$ and LiTaO$_3$ in backscattering detection geometry. In this case, nine transverse modes (E$_T$) for both parallel (i.e., $\langle z|xx|\bar{z}\rangle$ and $\langle z|yy|\bar{z}\rangle$) and perpendicular (i.e., $\langle z|yx|\bar{z}\rangle$ and $\langle z|xy|\bar{z}\rangle$) polarization settings of the pump and the probe light are possible. The four longitudinal $A_l$ modes should appear only for parallel polarization. Owing to the large numerical aperture of the objective, these strict rules are somewhat relaxed. Nevertheless, the technique is sensitive to changes in the local symmetry. **Figure 17** shows Raman spectra and the changes of the weak TO$_9$ mode across a domain wall. It is remarkable that changes occur only in this mode and not in any other. The data were obtained for a periodically poled congruent sample that was annealed at $T = 200°C$. The TO$_9$ mode expected in this spectral region is usually very weak owing to the symmetry of the involved Nb-O vibration. Apparently, this symmetry is perturbed by the presence of a domain wall.

## 4.5. Scanning Probe Microscopy Investigations Across a Domain Wall

SPM techniques offer very high spatial resolution that, although not as high as for TEM-based techniques, has been successfully applied to the imaging of the domain wall. Soergel (94) has previously reviewed the primary methods to detect domain walls by scanning probe techniques. Most of these AFM techniques rely on detecting manifestations of the domain—such as surface charges or changes in piezoelectric or dielectric response—with a sharpened cantilever that is scanned on the surface.

Piezoelectric force microscopy (PFM) has been used to study the antiparallel domain states of bulk crystals like triglycine sulfate (95, 96), $BaTiO_3$ (97, 98), and thin film piezoelectric samples of random domain orientations (99, 100). Briefly, the technique measures small piezoelectrically induced surface oscillations that are induced by an AC voltage applied to the surface through a conductive tip. Across a $180°$ domain wall, the sign of the piezoelectric coefficient $d_{33}$ changes, giving rise to a $\pi$ phase shift in piezodisplacements across the wall. The piezo-amplitude drops at the center of the wall, at which, in a classic picture, polarization goes to zero (see **Figure 18**).

The widths of the measured piezoresponses across domain walls in $LiNbO_3$ and $LiTaO_3$, as determined from the piezoelectric amplitude of the PFM image, are in the range of 65–150 nm (23, 25, 101, 102). This is strongly affected by both the tip radius and the sample thickness; smaller radii and thinner samples result in the narrowest widths (23, 25, 102, 103). Tian (25) performed a systematic study of wall width as a function of tip radius and tip shape. Experiments showed that FWHM ($x_{FWHM}$, indicating a $\pm 50\%$ transition) and FW ($x_{FW}$, indicating a $\pm 90\%$ transition) widths, in nanometers, of a domain wall were linearly related to the disk tip radius (radius of
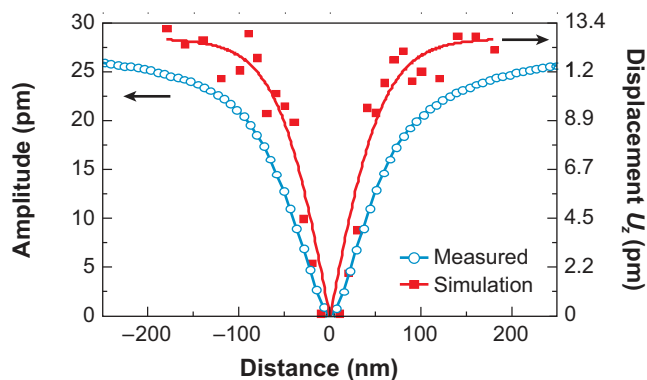


**Figure 18**

Vertical amplitude piezoelectric force microscopy signal on near-stoichiometric $LiNbO_3$ along with finite element method simulation results for a step domain wall. A 50-nm tip separated 0.1 nm from the surface with a bias of $\pm 5$ volts was assumed for modeling (23). Further work by Tian (25) indicates that a disk model for the tip without any spacing from the surface is more realistic. Reprinted with permission from Reference 23. Copyright (2005) by the American Physical Society.

the contact area $R$ in nanometers) by the following relationships:

$$x_{FWHM} = 7.2(\pm 3.14) + (\pm 0.09)R, \qquad\qquad 4.$$

$$x_{FW} = 79(\pm 10) + 3.95(\pm 0.1)R. \qquad\qquad 5.$$

The wall width increases linearly with the radius of the tip. Because the piezo-electric coefficient is directly proportional to polarization, these results suggest that, in addition to a narrow wall of >10 nm, there may be an intrinsic broadening of the polarization across the wall on the 79-nm scale.

Scanning nonlinear dielectric microscopy is another contact SPM technique. In this technique, a giga-Hertz signal applied to the surface through the AFM tip is used to measure changes in capacitance of the sample. The resolution and depth sensitivity are related to the order of the nonlinear dielectric constant being probed and become more concentrated with increasing order of nonlinear dielectric constant (104–106). This technique has measured a surface paraelectric layer on the surface of periodically poled $LiNbO_3$ with a depth of 0.75 nm and 2.75 nm that spontaneously forms on the crystal's surface with time (104). In periodically poled $LiNbO_3$, very strong residual stresses or electric fields that reduce the nonlinear dielectric constant in the region of the wall remain in the crystal (105). Annealing reduced these stresses, which allows a threefold increase in the strength of the nonlinear dielectric response. Additionally, the measured width of the domain wall in the stoichiometric crystals is much narrower than in the congruent crystals, which has been attributed to the stress caused by the defects in the congruent crystals (106). Scanning nonlinear dielectric microscopy (SNDM) has visualized the smallest domain features in the $LiNbO_3$ family of materials (~6 nm in stoichiometric $LiTaO_3$) (107). Obviously the total domain size is much smaller than the narrowest domain wall widths that have been measured with PFM, which is possible if only phase change across a wall is imaged. A recent SNDM study of domain walls in $LiTaO_3$ shows a minimum domain wall thickness of ~5.3 nm on the surface and ~1.2 nm in the bulk, consistent with PFM studies of a narrow wall component (107a).

## 4.6. Relationship between Electrical, Elastic, and Optical Properties Across a Domain Wall

**Table 2** summarizes all the unusual effects observed in the vicinity of a domain wall and their measured magnitudes in $LiNbO_3$. A key fact to remember in studying various properties in ferroelectrics, and particularly in domain walls here, is that all of them are interconnected. Cross-coupled effects between strain and electric fields (the piezoelectric and electrostrictive effects), electric fields and index changes (the electro-optic effect), and index changes and strain (the elasto-optic effect) need to be considered in constructing a complete picture of the domain wall. In this section, we attempt to bring together the different measurements described above.

For a virgin crystal, defect dipoles, such as those shown in **Figure 1**, have the most stable configuration. In contrast, domains created by an external electric field

**Table 2  Summary of local properties at a domain wall in lithium niobate (LiNbO$_3$) and lithium tantalate (LiTaO$_3$)**

| Property, technique (resolution) | Length scale for response width | Reference(s) | Congruent LiNbO$_3$ or LiTaO$_3$ | Annealed LiNbO$_3$ or LiTaO$_3$ |
|---|---|---|---|---|
| Refractive index change, $\Delta n_o$ (R-V), from NSOM[a] (100 nm) | 20 μm<br>2 μm | 19 | $10^{-3}$ (bulk)<br>$-5.5 \times 10^{-3}$ (wall) | $<10^{-5}$ |
| Birefringence, $B = \|n_{o,//}-n_{o\perp}\|$, from NSOM (100 nm) | 3–5 μm | 83 | $1.2 \times 10^{-4}$ (LiTaO$_3$) | $<10^{-5}$ (LiTaO$_3$) |
| Elastic strains by X-ray synchrotron ($\sim$1–6 μm) | 10–50 μm | 20, 21 | $\varepsilon 2 \sim -4 \times 10^{-5}$<br>$\varepsilon 5 \sim -5 \times 10^{-5}$<br>$\varepsilon 4 \sim 0$<br>$\varepsilon 3 \sim d_{33}E_3$ | $<10^{-6}$ (all) |
| Local electric fields (kV mm$^{-1}$) from polarization hysteresis (-), optical spectroscopy (300 nm), and NSOM (100 nm) | $\sim$22 μm<br>$\sim$4 μm | This paper | $E_3$ ($\|$ V) > 10 (bulk)<br>$E_3$ ($\|$ V) > 16 (wall)<br>$E_2 \sim 20$ (LiTaO$_3$) | $E_3 \sim 4$ (bulk)<br>$E_3 \sim 10$ (wall) |
| Phonon modes, Raman (500 nm) | 1.5 μm FWHM | This paper | Intensity increase of TO$_9$ mode at the wall | Unchanged |
| Electromechanical response by PFM (nanometer resolution; scales linearly with tip radius) | $\sim$1–70 nm | 23, 25 | Slight asymmetry in wall profile | (Extrapolation to zero tip radius limit) 1.8–8.5 nm (FWHM) 35–68 nm (FW) |

[a]NSOM, near-field scanning optical microscopy.

at room temperature consist of frustrated defect structures, which make this domain state relatively less stable than the virgin state. The defect field $E_3$ between the bulk of the R and V domain states measured through switching fields (Section 3), optical birefringence (Section 4.1), and Er probes (Section 4.3) is in the range of $-7$ to $-16$ kV mm$^{-1}$ in LiNbO$_3$. This field is biased antiparallel to the domain-inverted state (R), as indicated by the negative sign. Very locally at the wall (within 2–4 μm), additional fields of up to $-3$ to $-7$ kV mm$^{-1}$ can exist, as probed by Er ions (Section 4.3), which amounts to $\sim-10$ to $-23$ kV mm$^{-1}$ within the wall region. In addition, via X-ray synchrotron studies and symmetry arguments, local strains in the vicinity of the domain wall were measured to be $\varepsilon_2 \sim -4 \times 10^{-5}$, where the negative sign indicates a larger lattice parameter of the (3,0,.,0) plane in the R state with respect to the V state. Furthermore, strain component $\varepsilon_5 \sim -5 \times 10^{-5}$. This leads to a rise in the surface of the $+P_s$ end of a hexagonal R domain state with respect to the $-P_s$ end of a V domain matrix. The domain wall lies in the $y$-$z$ plane, and therefore by symmetry one expects $\varepsilon_4 \sim 0$. The internal strains and electric fields are related through the piezoelectric and electrostrictive effects.

The strains give rise to a change in the ordinary index, $n_o$ ($\equiv n_1 = n_2$), directly through the direct elasto-optic effect, given by $\Delta(1/n_1^2) = p_{1j}\varepsilon_j$. The strains also give rise to electric fields $E_j$ through the piezoelectric effect, $\varepsilon_i = d_{ji}E_j$, which in

turn give rise to a secondary index change through the electro-optic effect, given by $\Delta(1/n_1^2) = r_{1j}E_j$. The sum total of the primary and secondary effects can be summarized for LiNbO$_3$ (with *3m* symmetry) as

$$\Delta\left(1/n_1^2\right) = (p_{12} - p_{11})\varepsilon_2 + (p_{13}d_{33} + r_{13} + 2p_{11}d_{31})E_3 + p_{14}\varepsilon_4. \qquad 6.$$

Here the relations $\varepsilon_1 = 2d_{31}E_3 - \varepsilon_2$, and $E_3 \sim \varepsilon_3/d_{33}$ hold. We now substitute for the appropriate coefficients, using bulk LiNbO$_3$ values (87, 108, 109): $p_{11} = 0.032$, $p_{13} = 0.069$, $p_{31} = 0.153$, $p_{12} = p_{21} = 0.063$, $r_{13} \sim 10$ pm V$^{-1}$, $d_{31} = -0.85$ to $-1$ pC N$^{-1}$, $d_{33} = 6$–$16$ pC N$^{-1}$. We estimate a maximum ordinary index change, $\Delta n_o = \Delta n_1 \sim -10^{-3}$, in the bulk domain state R with respect to the bulk domain state V. In addition, a localized index change within 4 μm width around the wall of $\Delta n_o = \Delta n_1 \sim +1.5 \times 10^{-3}$ is predicted. These values compare very favorably with an overall change of $10^{-3}$ between the two domain states far from the wall and of $3 \times 10^{-3}$ at the wall itself, as measured earlier with NSOM (see **Figure 10**).

## 5. CONCLUSIONS AND FUTURE DIRECTIONS IN SCIENCE AND TECHNOLOGY

Unlike magnetic walls, ferroelectric walls are assumed, without much second thought, to be sharp on a unit cell level. The central message of this review is that this picture of ideality needs to be revisited in real life. Small amounts of nonstoichiometry and defects can alter the local wall structure dramatically, leading to order-of-magnitude changes on macroscale properties as well. This review shows that real domain walls have property changes on multiple distinctive length scales ranging from <10 nm, 50–100 nm, 2–4 μm, and 10–30 μm. Although these effects may be dismissed as extrinsic, they are real and dramatic and will influence the behavior of any real ferroelectric. For example, the polarization variation on the 50-nm scale in LiNbO$_3$ is as much as 20–27% of the bulk value.

The review focuses on trigonal ferroelectrics, but the results and questions raised appear to be far more general. Antiparallel domain walls are present in all ferroelectrics, and so are defects and defect clusters (110–118). Defect–domain wall interaction is therefore a very important area of research that deserves increased activity. An important element of this inquiry has to include atomistic simulations of the defect structures residing inside a wall. Very few such studies exist (10, 11). Because these defects can be extended, and because the unit cell in LiNbO$_3$ is large, one may have to resort to pseudopotential models for the material (119–122).

Furthermore, one needs to carefully define what one means by domain wall width. Is it defined in terms of polarization or in terms of other property variations across the wall? As shown above, there are multiple length scales over which these phenomena can be observed with varying sensitivities, depending on the probing method. Thus, the resolution and sensitivity limits of the probing method must be carefully considered.

Finally, one needs to consider whether there is any expected intrinsic broadening of the properties across the wall on larger length scales. In other words, would the wall show any property changes even without the presence of defects or defect clusters in

the lattice? One mechanism for apparent broadening of a wall is the spatial excursions of the wall that can give rise to a temporal averaging, leading to a broader wall (83). Such broadening would occur on a ∼5-nm length scale. A second more significant source of broadening is dynamical effects, in which the wall width changes under external stimuli. Is the wall width different when an external electric field is applied to the ferroelectric, thus deforming its Landau energy potential? From preliminary theory and experiments, the answer appears to be yes. We can approach this idea from two regimes: the applied field lower than coercive field, and the applied field higher than the coercive field for domain reversal and wall motion.

Does the broadening occur as the applied field approaches the coercive field for domain wall motion from the low-field direction? If so, the coercive field itself may be a dynamical property that is determined by the electric field broadening of the domain wall that lowers the coercive field for the motion of the wall. If we consider the presence of domain walls as a type of "defect" in the material, then the threshold field for the motion of this wall will define the coercive field. When the applied electric field broadens the wall to an extent that the coercive field is equal to the applied field, it may define the coercive field. Preliminary time-dependent GLD simulations (A. Choudhury & L.Q. Chen, personal communications) in $LiNbO_3$ show that the presence of a single $180°$ domain wall of only 2 nm width can lower the coercive field for domain reversal by two orders of magnitude. However, domain walls may not be the only "defects" in the material. The presence of pinning defects leads to bending and bowing of domain walls well below the coercive field (34), suggesting that coercive fields in such cases are pinning-depinning transitions. Does the wall broaden as it bows out between two pinning sites under an external field?

When the applied field is higher than the coercive field, the wall begins to move. How wide are moving domain walls, and is that field dependent? Experiments described in Section 4.3 show that moving walls can be up to four times wider than static walls and appear to have an extended influence up to 16 μm in width in $LiNbO_3$. Preliminary time-dependent GLD simulations of $180°$ domain walls in lead titanate indicate that moving walls under electric field broaden by two to four times from their static structure and wall widths increase by up to 10–30% under high fields in $LiNbO_3$ (A. Choudhury & L.Q. Chen, personal communications). This phenomenon is expected to be general.

These fundamental issues have not been addressed so far and provide much food for thought in the coming years. On the technology front, unlike magnetic domain wall–based technologies, which are commonplace today, the manipulation of ferroelectric domains into diverse shapes on various length scales to exploit a rich array of optical and memory technologies is still relatively undertapped. Hopefully the development of such promising technologies will follow with a better understanding of ferroelectric domain walls in the future.

## ACKNOWLEDGMENTS

## LITERATURE CITED

1. Lines ME, Glass AM. 1977. *Principles and Applications of Ferroelectrics and Related Materials*. Oxford, UK: Clarendon Press. 680 pp.
2. Gopalan V, Schepler KL, Dierolf V, Biaggio I. 2007. Ferroelectric materials. In *Handbook of Photonics*, ed. MC Gupta, J Ballato, 6:1–67. London: CRC Press
3. Gahagan KT, Gopalan V, Robinson JM, Jia QZX, Mitchell TE, et al. 1999. Integrated electro-optic lens/scanner in a LiTaO$_3$ single crystal. *Appl. Opt.* 38:1186–90
4. Batchko RG, Shur VY, Fejer MM, Byer RL. 1999. Backswitch poling in lithium niobate for high-fidelity domain patterning and efficient blue light generation. *Appl. Phys. Lett.* 75:1673–75
5. Kittel C. 2004. *Introduction to Solid State Physics*. New York: John Wiley and Sons. 704 pp. 8th ed.
6. Zhirnov VA. 1959. A contribution to the theory of domain walls in ferroelectrics. *Sov. Phys. JETP* 8:822–25
7. Gordon A. 1983. Tricritical phase-transitions in ferroelectrics. *Physica B & C* 122:321–22
8. Cao W, Barsch GR, Krumhansl JA. 1990. Quasi-one-dimensional solutions for domain walls and their constraints in improper ferroelastics. *Phys. Rev. B* 42:6396–401
9. Poykko S, Chadi DJ. 1999. Ab initio study of 180° domain wall energy and structure in PbTiO$_3$. *Appl. Phys. Lett.* 75:2830–32
10. Padilla J, Zhong W, Vanderbilt D. 1996. First-principles investigation of 180° domain walls in BaTiO$_3$. *Phys. Rev. B* 53:R5969–73
11. Meyer B, Vanderbilt D. 2002. Ab initio study of ferroelectric domain walls in PbTiO$_3$. *Phys. Rev. B* 65:104111/1–11
12. Foeth M, Sfera A, Stadelmann P, Buffat PA. 1999. A comparison of HREM and weak beam transmission electron microscopy for the quantitative measurement of the thickness of ferroelectric domain walls. *J. Electron Microsc.* 48:717–23
13. Huang XR, Hu XB, Jiang SS, Feng D. 1997. Theoretical model of 180° domain-wall structures and their transformation in ferroelectric perovskites. *Phys. Rev. B* 55:5534–37
14. Shilo D, Ravichandran G, Bhattacharya K. 2004. Investigation of twin-wall structure at the nanometre scale using atomic force microscopy. *Nat. Mater.* 3:453–57

15. Bursill LA, Lin PJ. 1986. Electron microscopic studies of ferroelectric crystals. *Ferroelectrics* 70:191–203

16. Hytch MJ, Snoeck E, Kilaas R. 1998. Quantitative measurement of displacement and strain fields from HREM micrographs. *Ultramicroscopy* 74:131–46

17. Stemmer S, Streiffer SK, Ernst F, Rühle M. 1995. Atomistic structure of 90° domain walls in ferroelectric PbTiO$_3$ thin films. *Philos. Mag. A* 71:713–24

18. Yang TJ, Gopalan V, Swart P, Mohideen U. 2000. Experimental study of internal fields and movement of single ferroelectric domain walls. *J. Phys. Chem. Solids* 61:275–82

19. Kim S, Gopalan V. 2005. Optical index profile at an antiparallel ferroelectric domain wall in lithium niobate. *Mater. Sci. Eng. B* 120:91–94

20. Kim S, Gopalan V, Steiner B. 2000. Direct X-ray synchrotron imaging of strains at 180° domain walls in congruent LiNbO$_3$ and LiTaO$_3$ crystals. *Appl. Phys. Lett.* 77:2051–53

21. Jach T, Kim S, Gopalan V, Durbin S, Bright D. 2004. Long-range strains and the effects of applied field at 180° ferroelectric domain walls in lithium niobate. *Phys. Rev. B* 69:064113/1–9

22. Dierolf V, Sandmann C. 2007. Combined excitation emission spectroscopy of defects for site-selective probing of ferroelectric domain inversion in lithium niobate. *J. Luminescence* 125:67–79

23. Scrymgeour DA, Gopalan V. 2005. Nanoscale piezoelectric response across a single antiparallel ferroelectric domain wall. *Phys. Rev. B* 72:24103/1–16

24. Kim S, Gopalan V, Kitamura K, Furukawa Y. 2001. Domain reversal and nonstoichiometry in lithium tantalate. *J. Appl. Phys.* 90:2949–63

25. Tian L. 2006. *Nanoscale probing and photonic applications of ferroelectric domain walls*. PhD thesis. Penn. State Univ., University Park

26. Kim S, Gopalan V, Gruverman A. 2002. Coercive fields in ferroelectrics: a case study in lithium niobate and lithium tantalate. *Appl. Phys. Lett.* 80:2740–42

27. Bandyopadhyay AK, Ray PC. 2004. Perturbation analysis and memory in ferroelectric materials. *J. Appl. Phys.* 95:226–30

28. He LX, Vanderbilt D. 2003. First-principles study of oxygen-vacancy pinning of domain walls in PbTiO$_3$. *Phys. Rev. B* 68:134103/1–7

29. Lee WT, Salje EKH, Bismayer U. 2005. Influence of point defects on the distribution of twin wall widths. *Phys. Rev. B* 72:104116/1–4

30. Abrahams SC, Bernstein JL. 1967. Ferroelectric lithium tantalate. 1. Single crystal X-ray diffraction study at 24°C. *J. Phys. Chem. Solids* 28:1685–92

31. Abrahams SC, Hamilton WC, Reddy JM. 1966. Ferroelectric lithium niobate. IV. Single crystal neutron diffraction study at 24°C. *J. Phys. Chem. Solids* 27:1013–18

32. Abrahams SC, Levinstein HJ, Reddy JM. 1966. Ferroelectric lithium niobate. V. Polycrystal X-ray diffraction study between 24° and 1200°C. *J. Phys. Chem. Solids* 27:1019–26

33. Abrahams SC, Reddy JM, Bernstein JL. 1966. Ferroelectric lithium niobate. III. Single crystal X-ray diffraction study at 24°C. *J. Phys. Chem. Solids* 27:997–1012

34. Gopalan V, Aust JA, Sanford NA, Kitamura K, Furukawa Y. 2000. Crystal growth, characterization, and domain studies in ferroelectric lithium niobate and tantalate. In *Handbook of Advanced Electronic and Photonic Materials and Devices*, ed. HS Nalwa, pp. 57–114. San Diego: Academic

35. Rauber A. 1978. Chemistry and physics of lithium niobate. In *Current Topics in Materials Science*, ed. E Kaldis, pp. 481–501. Amsterdam: North-Holland

36. Prokhorov AM, Kuzminov IUS. 1990. *Physics and Chemistry of Crystalline Lithium Niobate*. Bristol/New York: Hilger. 377 pp.

37. Scrymgeour DA, Gopalan V, Itagi A, Saxena A, Swart PJ. 2005. Phenomeno-logical theory of a single domain wall in uniaxial trigonal ferroelectrics: lithium niobate and lithium tantalate. *Phys. Rev. B* 71:184110/1–13

38. Kitamura K, Yamamoto JK, Iyi N, Kimura S, Hayashi T. 1992. Stoichiometric $LiNbO_3$ single crystal growth by double crucible Czochralski method using automatic powder supply system. *J. Cryst. Growth* 116:327–32

39. Kitamura K, Furukawa Y, Niwa K, Gopalan V, Mitchell TE. 1998. Crystal growth and low coercive field 180° domain switching characteristics of stoi-chiometric $LiTaO_3$. *Appl. Phys. Lett.* 73:3073–75

40. Tian L, Gopalan V, Galambos L. 2004. Domain reversal in stoichiometric $LiTaO_3$ prepared by vapor transport equilibration. *Appl. Phys. Lett.* 85:4445–47

41. Bordui PF, Norwood RG, Jundt DH, Fejer MM. 1992. Preparation and char-acterization of off-congruent lithium niobate crystals. *J. Appl. Phys.* 71:875–79

42. Kitamura K, Furukawa Y, Niwa K, Gopalan V, Mitchell TE. 1998. Crystal growth and low coercive field 180° domain switching characteristics of stoi-chiometric $LiTaO_3$. *Appl. Phys. Lett.* 73:3073–75

43. Gopalan V, Mitchell TE, Furukawa Y, Kitamura K. 1998. The role of non-stoichiometry in 180° domain switching of $LiNbO_3$ crystals. *Appl. Phys. Lett.* 72:1981–83

44. Gopalan V, Gupta MC. 1996. Observation of internal field in $LiTaO_3$ single crystals: its origin and time-temperature dependence. *Appl. Phys. Lett.* 68:888–90

45. Gopalan V, Mitchell TE, Kitamura K, Furukawa Y. 1998. The role of sto-ichiometry in 180° domain switching in $LiNbO_3$ crystals. *Appl. Phys. Lett.* 72:1981–83

46. Tian L, Gopalan V. 2004. Domain reversal in stoichiometric lithium tantalate prepared by vapor transport equillibration. *Appl. Phys. Lett.* 85:4445–47

47. Smyth DM. 1983. Defects and transport in $LiNbO_3$. *Ferroelectrics* 50:93–102

48. Schirmer OF, Thiemann O, Woehlecke M. 1991. Defects in $LiNbO_3$. I. Ex-perimental aspects. *J. Phys. Chem. Solids* 52:185–200

49. Abrahams SC, Marsh P. 1986. Defect structure dependence on composition in lithium-niobate. *Acta Crystallogr. B* 42:61–68

50. Donnerberg H, Schirmer OF, Catlow CRA, Tomlinson SM. 1991. Computer simulation of extrinsic defects in $LiNbO_3$ crystals. *Radiat. Eff. Defects Solids* 119–121:957–62

51. Lerner P, Legras C, Dumas J. 1968. Stoechiometrie des monocristaux de metaniobate de lithium. *J. Cryst. Growth* 3/4:231–35

52. Iyi N, Kitamura K, Izumi F, Yamamoto JK, Hayashi T, et al. 1992. Comparative study of defect structures in lithium niobate with different compositions. *J. Solid State Chem.* 101:340–52

53. Zotov N, Boysen H, Frey F, Metzger T, Born E. 1994. Cation substitution models of congruent $LiNbO_3$ investigated by X-ray and neutron powder diffraction. *J. Phys. Chem. Solids* 55:145–52

54. Zotov N, Frey F, Boysen H, Lehnert H, Hornsteiner A, et al. 1995. X-ray and neutron diffuse scattering in $LiNbO_3$ from 38 to 1200 K. *Acta Crystallogr. B* B51:961–72

55. Ivanova EM, Sergeev NA, Yatsenko AV. 1998. Analysis of intrinsic defects in the lithium niobate structure by the NMR $^7Li$ method. *Kristallografiya* 43:337–40

56. Yatsenko AV, Ivanova EN, Sergeev NA. 1997. NMR study of intrinsic defects in congruent $LiNbO_3$. 1. "Unoverlapping" defects. *Physica B* 240:254–62

57. Yatsenko AV, Ivanova-Maksimova HM, Sergeev NA. 1998. NMR study of intrinsic defects in congruent $LiNbO_3$. 2. "Overlapping" defects. *Physica B* 254:256–59

58. Zhdanov GS, Kolontsova EV, Korneev AE, Ivanov SA. 1978. X-ray diffuse scattering from single crystal $LiNbO_3$ and $LiTaO_3$ as a function of temperature between 20–750°C. *Ferroelectrics* 21:463–65

59. Ivanov SA, Korneev AE, Kolontsova EV, Venevtsev YN. 1978. Temperature dependence of intensity of diffuse X-ray scattering in single crystals of $LiTaO_3$. *Kristallografiya* 23:1071–73

60. Arlt G, Neumann H. 1988. Internal bias in ferroelectric ceramics: origin and time dependence. *Ferroelectrics* 87:109–120

61. Lambeck PV, Jonker GH. 1977. Ferroelectric domain stabilization in $BaTiO_3$ by bulk ordering of defects. *Ferroelectrics* 22:729–31

62. Warren WL, Pike GE, Vanheusden K, Dimos D, Tuttle BA, Robertson J. 1996. Defect-dipole alignment and tetragonal strain in ferroelectrics. *J. Appl. Phys.* 79:9250–57

63. Bergmann G. 1968. The electrical conductivity of $LiNbO_3$. *Solid State Commun.* 6:77–79

64. Gopalan V, Gupta MC. 1997. Origin and characteristics of internal fields in $LiNbO_3$ crystals. *Ferroelectrics* 198:49–59

65. Nassau K, Lines ME. 1970. Stacking-fault model for stoichiometry deviations in $LiNbO_3$ and $LiTaO_3$ and the effect on the Curie temperature. *J. Appl. Phys.* 41:533–37

66. Battle CC, Kim S, Gopalan V, Barkocy K, Gupta MC, et al. 2000. Ferroelectric domain reversal in congruent $LiTaO_3$ crystals at elevated temperatures. *Appl. Phys. Lett.* 76:2436–38

67. Scrymgeour DA. 2004. *Local Structure and Shaping of Ferroelectric Domain Walls for Photonic Applications*. PhD thesis. Penn. State Univ., University Park. 294 pp.

68. Leng S, Yu Y. 1994. Bulk and surface resistivity of $LiNbO_3$ and $LiTaO_3$ crystals versus temperature. *Phys. Status Solid. A* 143:431–39

69. Kovacs L, Polgar K. 2002. Electrical conductivity of $LiNbO_3$. In *Properties of Lithium Niobate*, ed. KK Wong, pp. 91–96. London: INSPEC, IEE

70. Blistanov AA, Geras'kin VV, Stepanova AV, Puchkova MV, Sorokin NG. 1984. Changes in the pyroelectric field and electrical conduction mechanisms in $LiNbO_3$ at T = 20–200°C. *Fiz. Tverd. Tela* 26:684–87

71. Bergman G. 1968. The electical conductivity of $LiNbO_3$. *Solid State Commun.* 6:77–79

72. Qi W, Shuyan L, Yansheng Y. 1996. Activation energy of small polarons and conductivity in $LiNbO_3$ and $LiTaO_3$ crystals. *Phys. Status Solid. B* 194:661–65

73. Eggert HA, Imbrock J, Baumer C, Hesse H, Kratzig E. 2003. Infrared holographic recording in lithium tantalate crystals by means of the pyroelectric effect. *Opt. Lett.* 28:1975–77

74. Leng S, Yu Y. 1994. Bulk and surface resistivity of $LiNbO_3$ and $LiTaO_3$ crystals versus temperature. *Phys. Status Solid. A* 143:431–39

75. Staebler DL, Amodei JJ. 1972. Thermally fixed holograms in $LiNbO_3$. *Ferroelectrics* 3:107–13

76. Yariv A, Orlov SS, Rakuljic GA. 1996. Holographic storage dynamics in lithium niobate: theory and experiment. *J. Opt. Soc. Am. B* 13:2513–23

77. Buse K, Breer S, Peithmann K, Kapphan S. 1997. Origin of thermal fixing in photorefractive lithium niobate crystals. *Phys. Rev. B* 56:1225–35

78. Vormann H, Weber G, Kapphan S, Kraetzig E. 1981. Hydrogen as origin of the thermal fixing in $LiNbO_3$:Fe. *Solid State Commun.* 40:543–45

79. Birnie DPI. 1993. Review analysis of diffusion in lithium niobate. *J. Mater. Sci.* 28:302–15

80. Halstead TK. 1970. Temperature dependence of the Li NMR spectrum and atomic motion in $LiNbO_3$. *J. Chem. Phys.* 53:3427–35

81. Zhang ZY, Zhu YY, Zhu SN, Ming NB. 1996. Domain inversion by $Li_2O$ out-diffusion or proton exchange followed by heat treatment in $LiTaO_3$ and $LiNbO_3$. *Phys. Status Solid. A* 153:275–79

82. Gopalan V, Gerstl SSA, Itagi A, Mitchell TE, Jia QX, et al. 1999. Mobility of 180° domain walls in congruent $LiTaO_3$ measured using real-time electro-optic imaging microscopy. *J. Appl. Phys.* 86:1638–46

83. Yang TJ, Gopalan V, Swart PJ, Mohideen U. 1999. Direct observation of pinning and bowing of a single ferroelectric domain wall. *Phys. Rev. Lett.* 82:4106–9

84. Agronin A, Rosenwaks Y, Rosenman G. 2006. Direct observation of pinning centers in ferroelectrics. *Appl. Phys. Lett.* 88:072911/1–3

85. Gopalan V, Gupta MC. 1996. Origin of internal field and visualization of 180° domains in congruent $LiTaO_3$ crystals. *J. Appl. Phys.* 80:6099–706

86. Kim S. 2003. *Optical, electrical, and elastic properties of domain walls in lithium niobate and lithium tantalate*. PhD thesis. Penn. State Univ., University Park

87. Yamada T. 1981. Data: $LiNbO_3$ family. In *Landolt-Bornstein New Series*, *Group III, Vol. 16*, ed. KH Hellwege, AM Hellwege, pp. 149–63. Berlin: Springer-Verlag

88. Dierolf V, Sandmann C. 2003. Confocal two photon emission microscopy: a new approach to waveguide imaging. *J. Lumin.* 102–103:201–5

89. Gog T, Griebenow M, Materlik G. 1993. X-ray standing wave determination of the lattice location of Er diffused into LiNbO$_3$. *Phys. Lett. A* 181:417–20

90. Dierolf V, Sandmann C, Gopalan V, Kim S, Polgar K. 2003. Ferroelectric domain imaging by defect luminescence microscopy. *J. Appl. Phys.* 93:2295–97

91. Deleted in proof

92. Dierolf V, Sandmann C, 2006. Role of extrinsic defects in ferroelectric domain inversion of lithium niobate. *Ceram. Trans.* 196:143–54

93. Dierolf V, Sandmann C. 2004. Inspection of periodically poled waveguide devices by confocal luminescence microscopy. *Appl. Phys. B* 78:363–66

94. Soergel E. 2005. Visualization of ferroelectric domains in bulk single crystals. *Appl. Phys. B* 81:729–52

95. Hong JW, Noh KH, Park SI, Kwun SI, Khim ZG. 1998. Surface charge density and evolution of domain structure in triglycine sulfate determined by electrostatic-force microscopy. *Phys. Rev. B* 58:5078–84

96. Likodimos V, Labardi M, Allegrini M, Garcia N, Osipov VV. 2001. Surface charge compensation and ferroelectric domain structure of triglycine sulfate revealed by voltage-modulated scanning force microscopy. *Surf. Sci.* 490:76–84

97. Kalinin SV, Bonnell DA. 2002. Imaging mechanism of piezoresponse force microscopy of ferroelectric surfaces. *Phys. Rev. B* 65:125408/1–11

98. Eng LM, Abplanalp M, Guenter P. 1998. Ferroelectric domain switching in tri-glycine sulfate and barium-titanate bulk single crystals by scanning force microscopy. *Appl. Phys. A* 66:679–83

99. Gruverman A, Auciello O, Tokumoto H. 1996. Scanning force microscopy for the study of domain structure in ferroelectric thin films. *J. Vac. Sci. Technol. B* 14:602–5

100. Lee K, Shin H, Moon WK, Jeon JU, Pak YE. 1999. Detection mechanism of spontaneous polarization in ferroelectric thin films using electrostatic force microscopy. *Jpn. J. Appl. Phys. 2* 38:L264–66

101. Wittborn J, Canalias C, Rao KV, Clemens R, Karlsson H, Laurell F. 2002. Nanoscale imaging of domains and domain walls in periodically poled ferroelectrics using atomic force microscopy. *Appl. Phys. Lett.* 80:1622–24

102. Rodriguez BJ, Nemanich RJ, Kingon A, Gruverman A, Kalinin SV, et al. 2005. Domain growth kinetics in lithium niobate single crystals studied by piezoresponse force microscopy. *Appl. Phys. Lett.* 86:012906/1–3

103. Felten F, Schneider GA, Saldana JM, Kalinin SV. 2004. Modeling and measurement of surface displacements in BaTiO$_3$ bulk material in piezoresponse force microscopy. *J. Appl. Phys.* 96:563–68

104. Ohara K, Cho Y. 2001. Fundamental study of surface layer on ferroelectrics by scanning nonlinear dielectric microscopy. *Jpn. J. Appl. Phys. 1* 40:5833–36

105. Cho Y, Kazuta S, Ito H. 2001. Scanning-nonlinear-dielectric-microscopy study on periodically poled LiNbO$_3$ for a high-performance quasi-phase matching device. *Appl. Phys. Lett.* 79:2955–57

106. Sugihara T, Cho Y. 2005. Investigation of three-dimensional domain structure in LiTaO$_3$ by scanning nonlinear dielectric microscopy. *Jpn. J. Appl. Phys. 1* 44:7169–73

107. Hiranaga Y, Cho Y, Fujimoto K, Wagatsuma Y, Onoe A. 2003. Ultrahigh-density ferroelectric data storage using scanning nonlinear dielectric microscopy. *Jpn. J. Appl. Phys. 1* 42:6050–54

107a. Daimon Y, Cho Y. 2006. Cross-sectional observation of nano-domain dots formed in congruent single crystal $LiTaO_3$. *Jpn. J. Appl. Phys.* 45:L1304–6

108. Weis RSFC. 2002. Photoelastic coefficients of $LiNbO_3$. In *Properties of Lithium Niobate*, ed. KK Wong, pp. 61–64. London: INSPEC, IEE

109. Dixon RW, Cohen MG. 1966. A new technique for measuring magnitudes of photoelastic tensors and its application to lithium niobate. *Appl. Phy. Lett.* 8:205–7

110. Zhang R, Li JF, Viehland D. 2004. Self-assembly of point defects into clusters and defect-free regions: a simulation study of higher-valent substituted ferroelectric perovskites. *Comput. Mater. Sci.* 29:67–75

111. XuDong F, Hua Q, JuLin P, Bursill LA. 1995. HRTEM analysis of nanodomain textures in PMN. *Integr. Ferroelectrics* 9:233–42

112. Vogt H. 1991. Evidence of defect-induced polarization clusters in nominally pure $KTaO_3$ from low-temperature Raman and hyper-Raman spectra. *J. Phys. Condens. Matter* 3:3697–709

113. Trepakov V, Smutny F, Vikhnin V, Bursian V, Sochava L, et al. 1995. The effects of defect system ordering in a weakly doped incipient ferroelectric ($KTaO_3$): dielectric manifestation. *J. Phys. Cond. Matter* 7:3765–77

114. Stashans A, Serrano S, Medina P. 2006. A quantum-chemical study of oxygen-vacancy defects in $PbTiO_3$ crystals. *Physica B* 381:82–89

115. Qi T, Xu Z, Jie-Fang L, Viehland D. 1997. Role of defect distributions and mobility on ferroelectric phase transformations in lead zirconate titanate. *Appl. Phys. Lett.* 71:1062–64

116. Keeble DJ, Nielsen B, Krishnan A, Lynn KG, Madhukar S, et al. 1998. Vacancy defects in (Pb, La)(Zr, Ti)$O_3$ capacitors observed by positron annihilation. *Appl. Phys. Lett.* 73:318–20

117. Ghosh VJ, Nielsen B, Friessnegg T. 2000. Identifying open-volume defects in doped and undoped perovskite-type $LaCoO_3$, $PbTiO_3$, and $BaTiO_3$. *Phys. Rev. B* 61:207–212

118. Poykko S, Chadi DJ. 2000. Ab initio study of dipolar defects and 180° domain walls in $PbTiO_3$. *J. Phys. Chem. Solids* 61:291–94

119. Phillpot SR, Gopalan V. 2004. Coupled displacive and order-disorder dynamics in $LiNbO_3$ by molecular-dynamics simulation. *Appl. Phys. Lett.* 84:1916–18

120. Tomlinson SM, Freeman CM, Catlow CRA, Donnerberg H, Leslie M. 1989. Atomistic simulation studies of technologically important oxides. *J. Chem. Soc. Faraday Trans. 2* 85:367–83

121. Donnerberg H, Tomlinson SM, Catlow CRA, Schirmer OF. 1989. Computer-simulation studies of intrinsic defects in $LiNbO_3$ crystals. *Phys. Rev. B* 40:11909–16

122. Donnerberg H, Tomlinson SM, Catlow CRA, Schirmer OF. 1991. Computer-simulation studies of extrinsic defects in $LiNbO_3$ crystals. *Phys. Rev. B* 44:4877–83

123. Kawas MJ, Stancil DD, Schlesinger TE, Gopalan V. 1997. Electrooptic lens stacks on LiTaO$_3$ by domain inversion. *J. Lightwave Technol.* 15:1716–19

124. Yu NE, Kurimura S, Nomura Y, Kitamura K. 2005. Stable high-power green light generation with a periodically poled stoichiometric lithium tantalate. *Mater. Sci. Eng. B* 120:146–49

125. Agronin A, Molotskii M, Rosenwaks Y, Rosenman G, Rodriguez BJ, et al. 2006. Dynamics of ferroelectric domain growth in the field of atomic force microscope. *J. Appl. Phys.* 99:104102/1–6

126. Baumer C, David C, Tunyagi A, Betzler K, Hesse H, et al. 2003. Composition dependence of the UV absorption edge in lithium tantalate. *J. Appl. Phys.* 93:3102–4

127. Yan W, Kong Y, Shi L, Sun L, Liu H, et al. 2006. Influence of composition on the photorefractive centers in pure LiNbO$_3$ at low light intensity. *Appl. Opt.* 45:2453–58

# Contents

**Index**

**Errata**

An online log of corrections to *Annual Review of Materials Research* chapters (if any,
1997 to the present) may be found at http://matsci.annualreviews.org/errata.shtml